

Self-organizing fluids for active building facades

Authors: Raphael Kay^{1,2,3*}, Charlie Katrycz¹, Kevin Nitièma³, J. Alstan Jakubiec^{3,4}, Benjamin D. Hatton¹

Affiliations:

¹Department of Materials Science and Engineering, University of Toronto; Toronto, Canada.

²Department of Mechanical and Industrial Engineering, University of Toronto; Toronto, Canada.

³John H. Daniels Faculty of Architecture, Landscape and Design, University of Toronto; Toronto, Canada

⁴School of the Environment, University of Toronto; 149 College Street, Toronto, Ontario, M5T 1P5.

*Corresponding author. Email: raphael.kay@mail.utoronto.ca

Typical buildings are static structures, unable to adjust to dynamic temperature and daylight fluctuations¹⁻³. Adaptive facades that are responsive to these unsteady solar conditions could substantially reduce operational energy inefficiencies, indoor heating, cooling, and lighting costs, as well as greenhouse-gas emissions^{4,5}. Inspired by marine organisms that disperse pigments within their skin⁶, we propose a new building interface that uses reversible fluid injections to tune optical transmission. Pigmented fluids with self-organizing morphologies are reversibly injected and withdrawn from confined layers, achieving locally-tunable shading and interior solar exposure. Multicell arrays tiled across large areas enable differential, dynamic building responses. Fluidic reconfigurations can find optimal states over time, replicating the behavior of biological tissue. Compared to the best available electrochromic technology, the presented fluidic facades can reduce heating, cooling, and lighting energy in our models by over 30%.

Biological organisms have evolved a vast collection of dynamic regulatory controls to maintain an equilibrium with their environment. As a remarkable example, Antarctic krill, *E. superba*, can actively change color within minutes depending on sunlight intensity for ultraviolet protection⁶. Like several decapods⁷⁻¹², krill store and disperse pigment throughout the cells within their skin, evolving a rapid and reversible response mechanism for solar shading (Fig. 1a-d)^{6,13,14}.

Buildings, in contrast, are generally unequipped to achieve adaptive solar shading responses, built with static outer facades, despite operating within highly variable temperature and light regimes¹⁻³. A skyscraper in a typical seasonal climate, for instance, might experience fluctuations in solar radiation from almost 0 to an astounding 800 W/m² within a day. Static glazing materials cannot regulate optical transmission in response to these fluctuating solar loads¹⁵. Unshaded windows, for instance, allow excessive solar heating in the summer when directly normal to the sun, contributing to high seasonal cooling energy costs¹⁻³. Windows with infrared-reflective and low-emissivity coatings, on the other hand, limit crucial solar ingress in the winter, and incur equally-consequential seasonal heating energy costs². Beyond heating effects, windows also must provide sufficient total interior illumination while limiting excessive localized glare⁵. Today, in large part because outer glazing materials cannot adaptively or locally shade against solar loads, buildings consume almost 75% of the U.S. national electricity supply¹⁶ and approximately one third of the global energy supply¹⁷. Adaptive glazing materials, capable of both dynamic and localized solar shading, have the potential to significantly improve energy efficiency for a recognizable impact on climate change^{4,5}, and could additionally reduce local glare to improve indoor human comfort^{18,19}.

Despite this potential impact^{4,20}, active shading in buildings has been difficult to achieve. An 'ideal' optically-active building facade should be locally-responsive (maximize light transmission, but limit glare), digitally-controllable (optimize material properties and building configuration), low-cost and scalable across large areas, while also energy-efficient to operate. Currently, many buildings only achieve shading through manual, large-scale, mechanical blinds^{21,22}. Rotating shading frits²³ and other automated mechanical structures^{24,25} have also been tested. However, these macroscale mechanical approaches are typically costly, slow, and have low spatial resolution^{1,26} for localized shading responses^{21,22}. Certain smart materials have also been developed for active shading, but have practical

limitations. Electrochromic systems, for instance, which use chemical redox reactions to control optical transmission, are expensive ($\$500\text{-}1000 \text{ USD/m}^2$)²⁷⁻³¹ and complex to manufacture^{28,29,32}, typically reliant on energy-intensive sputter-deposition processes³³, restricting market viability^{3,27-29,34}. More experimental chromogenic systems that use electrically-reorientable liquid-crystals³⁵⁻³⁷ and suspended-particles^{38,39}, as well as active polymers that leverage dielectric elastomer actuations⁴⁰⁻⁴², require a continuous energy supply to maintain a 'bleached' state. Finally, stimulus-responsive materials and actuators (e.g., photochromics^{3,28,35,43-45}, thermochromics^{3,28,43-47}, and hygroscopics^{48,49}) suffer functional restrictions of their own^{28,41}, and cannot be digitally controlled or decoupled from their unique environmental triggers, limiting both the capacity for digital information processing and tunable user control.

Confined Fluidic Responses in Biology

In contrast, biological organisms often leverage tissue-scale fluidic mechanisms to regulate interfacial properties within evolving environments. Mammals dilate blood vessels near their skin to control rates of convective heat loss⁵⁰⁻⁵³; cephalopods stretch fluid-containing sacs to generate colorful displays for adaptive camouflage and visual communication⁵⁴⁻⁵⁹; brittle stars transport fluidic cells between sub-surface regions to regulate photoreception⁶⁰; and decapods (e.g., krill, crab) move pigments within their skin⁷⁻¹² to thermoregulate and dynamically shade against the sun^{6,61}. In low-light conditions, krill store pigments in a central reservoir within sub-surface chromatophore cells. Under intense light exposure, they then quickly (< 20 minutes) spread pigment through the radially-branching microtubules of the chromatophore, expanding the diameter of pigment coverage from <100 μm within the reservoir to >500 μm when expanded across the cell (Fig. 1a-b). In aggregate, this extended pigment fluid coverage significantly changes the optical properties of the skin (Fig. 1a-b)⁶. Crucially, only a small volume of fluid is required to actively and efficiently shade a large surface region, expanding from a point (reservoir) to an area.

We hypothesize that this intracellular actuation of confined fluidic pigment, scaled up as a material layer within a building facade, can replicate the dynamic optical response of biological tissue (Fig. 1g-j). Here, we combine principles of microfluidics, self-assembly, and digital actuation to conceptualize a large area building interface that can differentially sense and react to local optical conditions. We show that pigment-containing fluids, confined within layered devices, can be injected and withdrawn (Fig. 2d) to control color and shading, interior light intensity, and temperature. The self-organizing morphology of these injected fluids is controlled through the non-equilibrium dynamics of branching instabilities. This mechanism allows us to demonstrate that building facades with adaptive and reversible fluidic shading can achieve unprecedented improvements to energy efficiency.

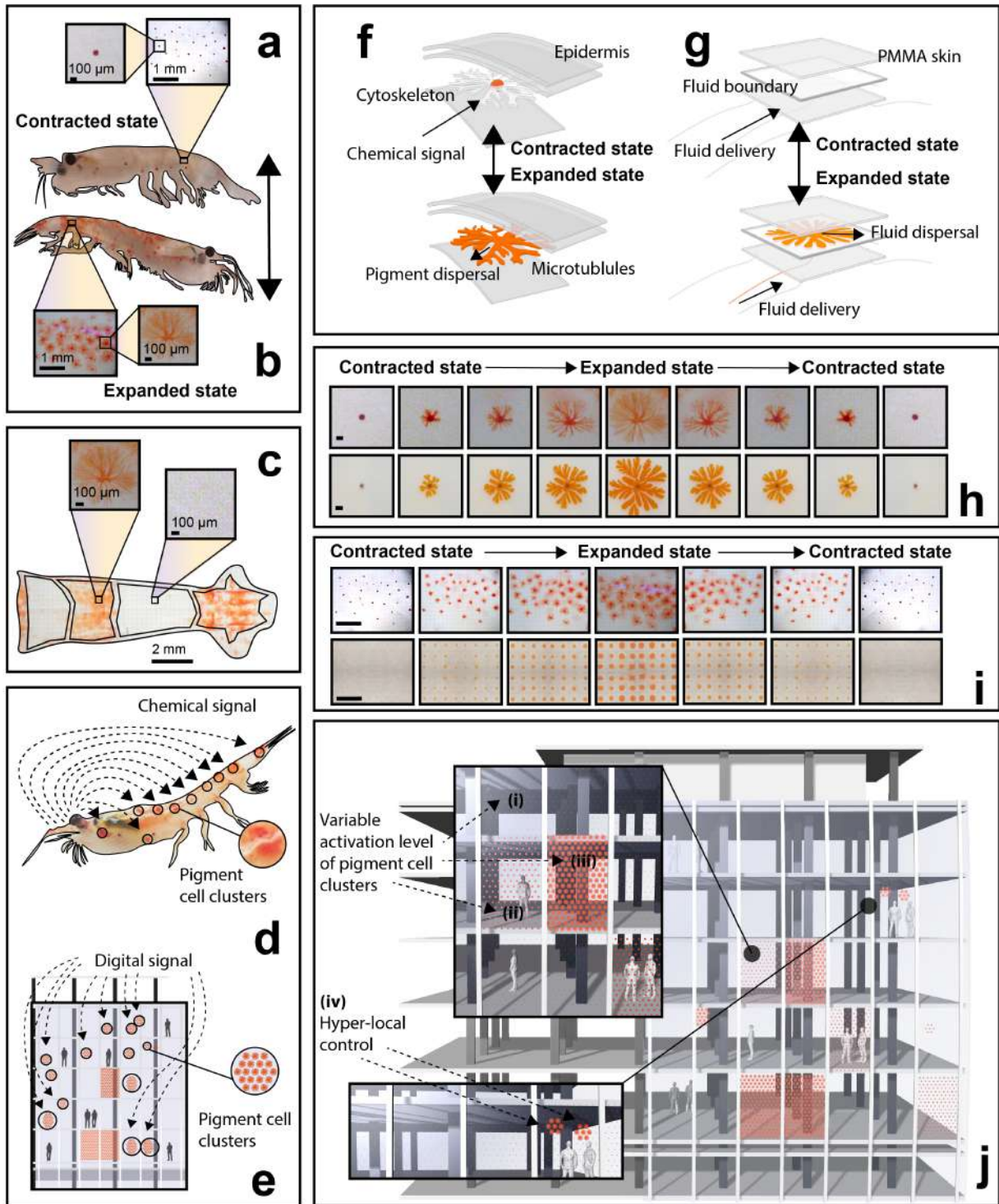


Fig. 1. Biological inspiration for active pigment fluid dispersal in buildings. (a-b) Reversible chromatophore activation in male Antarctic Krill when unexposed (a) and exposed to light (b) as a mechanism for dynamic solar shading. (c) Localized control over chromatophore coverage of the abdominal segments in Krill. (d-e) Schematic comparing the activation pathways for both biological chromatophore clusters in Krill (d) and synthetic chromatophore clusters in buildings (e), to control the ingress of solar radiation through the skin of Krill (d) and facade of buildings (e). (f-g) Exploded perspectival cross-section showing both the contracted (top) and expanded (bottom) state of a single chromatophore in both Krill (f) and synthetic device (g). (h) Images comparing complete

chromatophore expansion and contraction sequence in both Krill (top) and synthetic device (bottom). Top scale bar is 100 μm . Bottom scale bar is 2 cm. (i) Images comparing complete expansion and contraction sequence for a cluster of chromatophores in both Krill (top) and synthetic device (bottom). Top scale bar is 1 mm. Bottom scale bar is 5 cm. Bottom image is stitched from four images of a 4x3 pixel array. (j) Render showing dynamic and localized synthetic chromatophore activation within a building facade, where multiple activation states (i, ii, iii) and hyper-local control (iv) can be achieved. All images of Antarctic Krill in a-d, h-i used with the permission of Lutz Auerwald.

Characteristic Branching Morphologies of Injected Fluids

Marine organisms use radially-branching vascular networks to disperse pigment within their skin. Branched area coverage increases the effective scale of pigment dispersion, where a small volume of pigment fluid can expand across a much larger surface area in a branched morphology compared to a uniform disk. Here, we generate radially-branching pigment fluid morphologies within layered devices for tunable optical transmission. We demonstrate reversible pigment coverage, from a point reservoir to a large area, analogous to pigment dispersal for optical control in the krill chromatophore cell (Fig. 1f-g).

We control branched morphologies through the viscous fingering (VF) effect (Fig. 2a-e, Supplementary Video 1). VF is a well-known mechanism for branched pattern formation, where interfacial instabilities grow as a less viscous fluid is forced under pressure into a more viscous fluid, while confined between two closely spaced plates⁶². This patterning has been widely demonstrated and characterized using the quasi-2D Hele-Shaw (H-S) cell⁶³⁻⁶⁸, where fluid parameters and cell geometry can be controlled to tune the morphology and planar area fraction of the invading fluid.

Within H-S cells, injection flow rate affects pressure at the interface between the two fluids, and can be controlled experimentally. At sufficient flow rates, this interface can expand in a budding and branching pattern, as the ‘guest’ fluid bifurcates to form fingers within the ‘host’ fluid. The curvature of this interface, if unstable, is locally amplified. For vertical H-S cells, with density-matched fluids (no buoyant forces, see⁶²), the unstable tip-splitting growth of fingers occurs when an ‘amplification factor’ of a specific finger width, $a_\lambda > 0$, for

$$(1) \quad a_\lambda = 3V\Delta n - \sigma \left(\frac{\pi b}{\lambda} \right)^2$$

Where $\Delta n = n_h - n_g$, n_h is the host fluid viscosity, n_g is the invading guest fluid viscosity, V is the interfacial velocity, b is the gap height between plates, σ is the interfacial surface tension, and λ is the finger width, or wavelength, of the instability⁶². Unstable branching tips will grow if the growth rate (left hand term) is large enough to overcome the smoothing-effect of surface tension on the decay rate (right hand term). However, if the direction of flow is reversed, we can expect the reversal of stability. The sign of a_λ changes, due to the change in flow direction (swapping the host and guest fluid viscosities), causing a net decay of finger amplitudes. This mechanism of stability reversal allows our design to be flow reversible: when driven in the forward direction (pigment injection), instabilities cause branching morphologies. When driven backwards (pigment withdrawal), the curvature-dampening effect allows for the coordinated collapse of the branched fluid network back to its source.

The width of the branches in the pattern is a critical design parameter that helps to control pigment fluid area fraction and, subsequently, light transmission. The critical finger width λ_c divides stable and unstable growth,

$$(2) \quad \lambda_c = \pi b \sqrt{\frac{\sigma}{3V\Delta n}}$$

Wavelengths less than λ_c are stabilized due to the increase in the decay term in equation (1). All wavelengths longer than λ_c are unstable, with a practical upper limit at the longest wavelength that can fit along the interface,

determined by the radius of the fluid injection (Extended Data Fig. 8). The most accelerated instability that is characteristic of the branched pattern, is characteristic wavelength,

$$(3) \quad \lambda^* = \sqrt{3}\lambda_c = \pi b \sqrt{\frac{\sigma}{V\Delta n}}$$

We developed H-S cells ($30 \times 30 \times 0.1 \text{ cm}^3$) using PMMA sheets (fabrication details in SM), and controlled reversible fluid injections through a central port and digital syringe pump. If we assume a stably expanding circular disk, the velocity of the fluid interface is linearly proportional to the injection flow rate, $V = \frac{Q}{2\pi r b}$ (derivation in SM). Therefore, injection flow rate (Q) can be used to modulate V , and the onset of branching instability (λ^*). Experimentally, Q is highly practical for establishing control over pigment morphology due to its digital tunability.

Based on equation (1), we chose two immiscible fluids – a transparent mineral oil (288 cP, 20°C) and aqueous carbon suspension (0.89 cP, 20°C) – as the host and guest phase, respectively. Low injection rates (e.g., 0.5 mL/min) of the aqueous pigment phase corresponded to patterns of decreased branching during dispersal (Fig. 2f, top row), while increasing flow rate increased branching (Fig. 2f, moving downwards, Fig. 2h). For a consistent dispersal radius within a H-S cell, differences in branching resulting from injection flow rate corresponded to disparities of up to 21% in pigment fluid area coverage, from 42% coverage for a highly-branched state (Fig. 2f, top row), up to a maximum of 63% coverage for a non-branching state (Fig. 2f, bottom row, Fig. 2h). The well-established linear relationship between characteristic wavelength and interfacial velocity⁶² is confirmed using equation (3) (Extended Data Fig. 5c). Systematic control of Δn (and $n_{\text{guest}}/n_{\text{host}}$) was also demonstrated to tune area fraction by 25% (for the same relative pigment fluid radius), from 45% to 70% coverage (Extended Data Fig. 3b). Other results demonstrating geometric control over viscous fingering to tune optical transmission are available in Extended Data Fig. 1-7.

Reversibility of Injections and Switchable Injection Stability

To avoid buoyant forces in vertically-oriented cells, the aqueous pigment phase was adjusted (by adding ethanol) to an equivalent density such that $\rho_a - \rho_o = 0$, where ρ_a , ρ_o are the densities of the aqueous and oil phases, respectively. To control conditions for branching, we assume that the largest wavelength that can be supported on a circle is $\lambda = \frac{c}{2} = \pi r$, where c is the circumference of a circle and r its radius. This minimal instability simply transforms a circle into an ellipse, with two crests (fingers) oriented on opposite poles of the major axis. Unstable branching growth will therefore occur for $\lambda_c < \lambda < \pi r$. Stable, non-branching fluid injections ($a_\lambda < 0$) occur when $\lambda_c = \pi r$, and can be accomplished within a vertical cell (Supplementary Video 4) by ensuring $3V\Delta n < \sigma \left(\frac{b}{r}\right)^2$, where r is the effective radius of the pigment injection within a H-S cell. Plotting $\sigma, \Delta n$ as in Extended Data Fig. 9, a binary phase space is shown, where $a_\lambda = 0$ defines a line through the origin, of slope $m = 3V \left(\frac{r}{b}\right)^2$, separating stable and unstable regions (Extended Data Fig. 9). For a H-S cell aspect ratio $\frac{b}{r}$, one can then control the degree of instability using any of $\sigma, \Delta n, V$ (Extended Data Fig. 8-9). We found that less branched morphologies were often better able to retract due to pinching effects in narrower fingers. And we observed perfect repeatability for injections of non-branching fluid morphologies across 100 cycles.

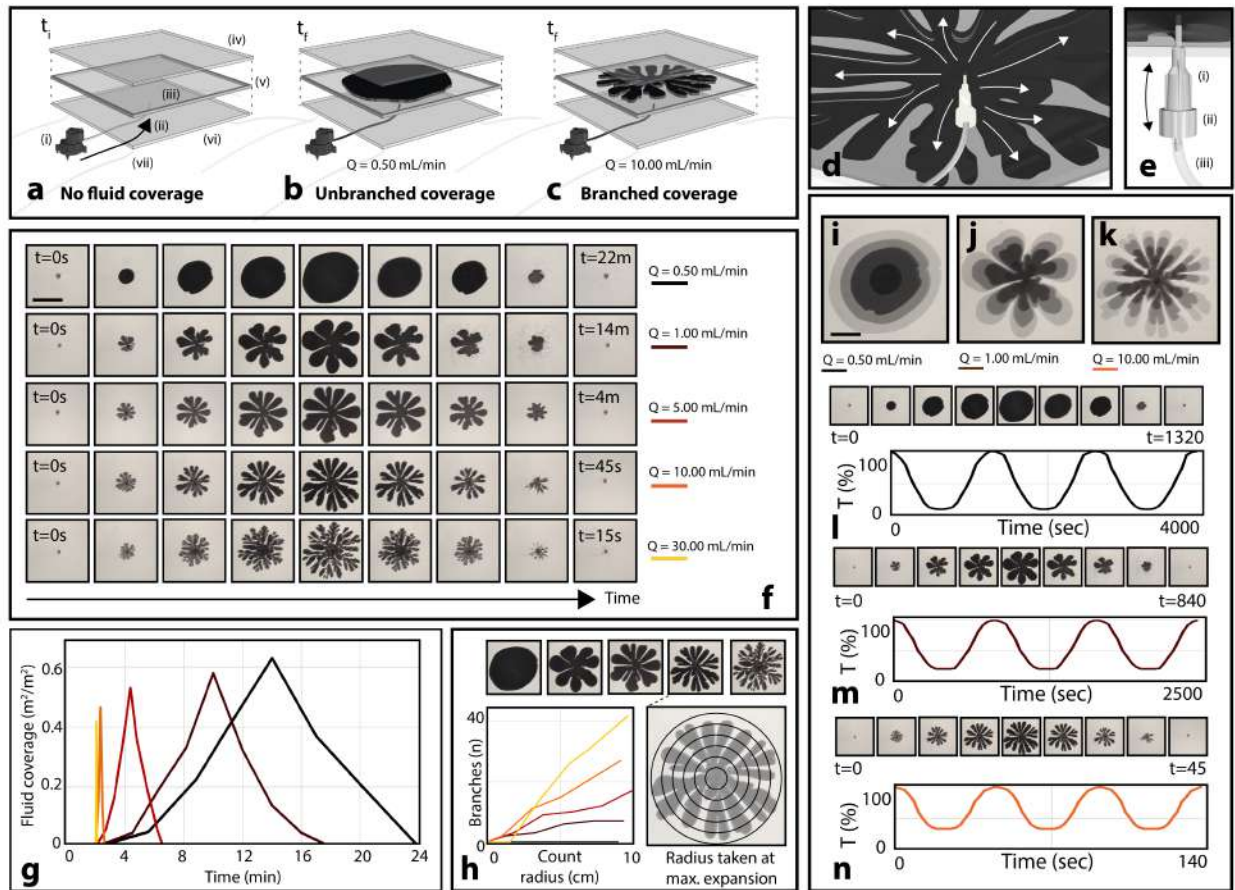


Fig. 2. Tuning shading coverage by actively controlling pigment fluid morphology. (a-c) Schematic of a single fluidic cell, with no pigment fluid coverage (a), unbranched pigment fluid coverage (b), and branched pigment fluid coverage (c). System components: (i) digitally controlled peristaltic pump; (ii) inward fluidic pigment flow with pressure; (iii) active fluidic pigment layer, 1 mm thick; (iv) first rigid plate; (v) outer gasket; (vi) second rigid plate; (vii) drain tubing for temporary fluid displacement. (d) Demonstrating the branching of pigment fluid when introduced at higher speed. (e) Inlet design: (i) needle; (ii) luer connector; (iii) hose connector. (f) Reversible pigment injection/withdrawal, where degree of branching is determined by injection flow rate (Q) from 0.5-30 mL/min. Scale bar is 15 cm. (g) Fluid coverage as a function of time for experiments pictured in (f). (h) The number of fluidic branches increases with flow rate. All measurements taken once pigment fluid fully dispersed. (i-k) Overlaid images of pigment fluid dispersal over time for three different flow rates. Scale bar is 5 cm. (l-n) Cyclical light transmission measurements across three pigment fluid dispersal and contraction cycles. Images represent first cycle. Light intensity varies for each system at full actuation. Because maximum light intensity was set to 100 lux, plots in (l-n) additionally display relative measured interior light intensity behind each cell in lux.

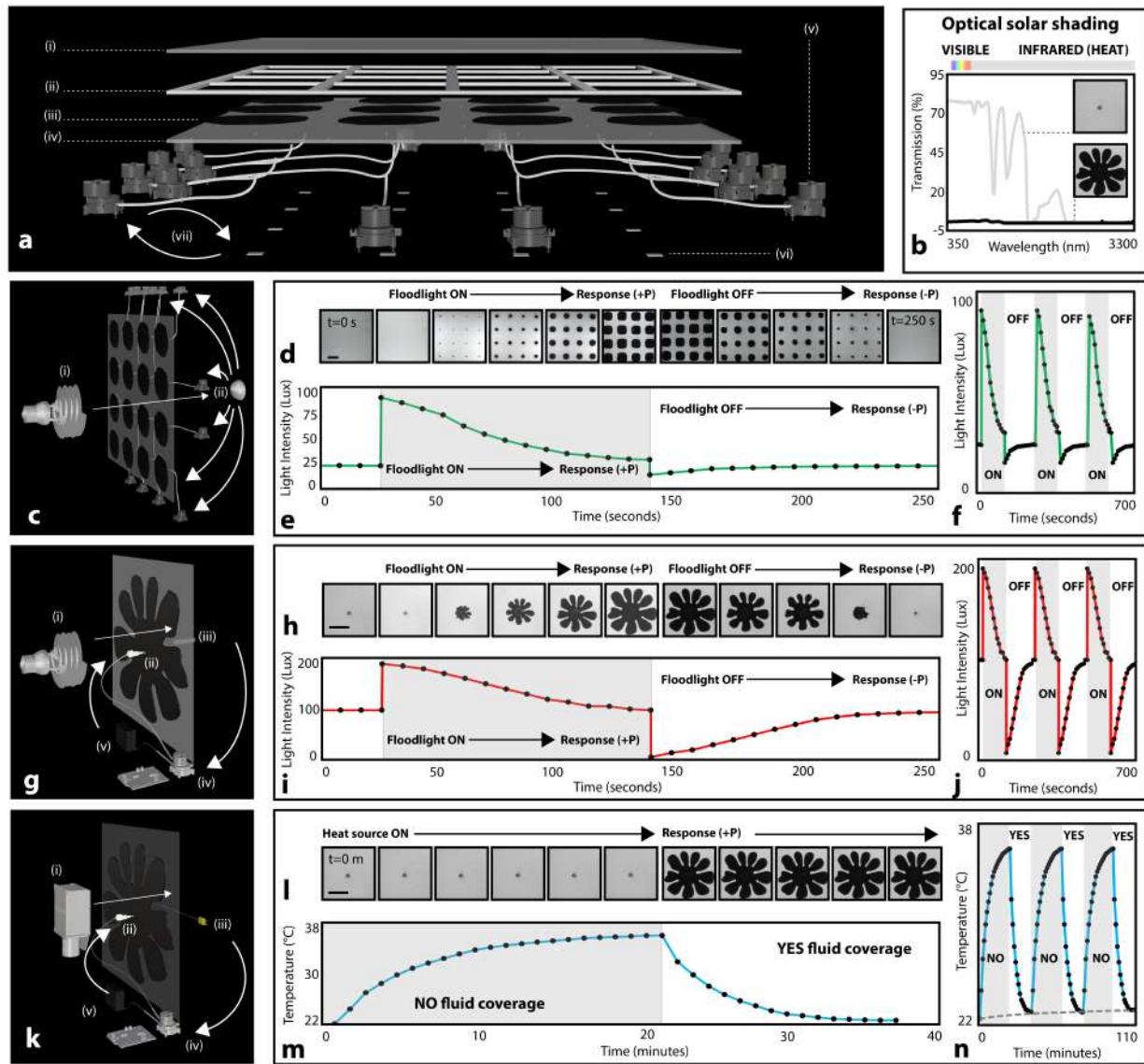


Fig. 3. Optical and thermal characterization of responsive pigment fluid dispersal for single and multicell system. (a) Multicell device: (i) outer expandable layer; (ii) adhesive and gasket; (iii) fluidic pigment layer; (iv) inner rigid plate; (v) digitally-driven peristaltic pump; (vi) light intensity sensor; (vii) feedback loop between sensor and pump. (b) Optical spectrum for pigment fluid (aqueous carbon black, black line) and castor oil (grey line). (c) Experimental setup for data in (d-f): (i) light source; (ii) single light sensor. (d) Images showing dispersal and contraction sequence for multicell devices as a response to light. Scale bar is 10 cm. (e) Light intensity as a function of time for single sequence in (d). (f) Three sequences of (e) to demonstrate consistency. (g) Experimental setup for data in h-j: (i) light source; (ii) dispersed pigment fluid layer; (iii) light sensor; (iv) signal to digital peristaltic pump; (v) control over pigment fluid dispersal. (h) Images showing dispersal and contraction sequence for single-cell device as a response to light. Scale bar is 15 cm. (i) Light intensity as a function of time for single sequence in (H). (j) Three sequences of (I) to demonstrate consistency. (k) Experimental setup for data in l-n: (i) heat source; (ii) dispersed pigment fluid layer; (iii) thermocouple measuring interior plate; (iv) signal to digital peristaltic pump; (v) control over pigment fluid dispersal. (l) Images showing dispersal and contraction sequence for single-cell facade as a response to temperature. Scale bar is 15 cm. (m) Temperature as a function of time for single sequence in (I). (n)

Three sequences of (m) to demonstrate consistency. Grey line represents control curve, where pigment fluid is dispersed statically across all three cycles.

Reversible Injection Tuning for Dynamic Shading

With well-defined control over branching stability, pigment fluid morphology, and pigment fluid reversibility, we demonstrated reversible, programmable pigment fluid injection to tune optical transmission and shading in H-S cells. In their transmissive (clear) state, cells contained a transparent fluid (mineral oil, 288 cP), enabling full transmission of visible light (Fig. 3b). To shade, we injected a less viscous pigment fluid (carbon black suspension in water-glycerol solution, 0.89-288 cP) into the mineral oil layer (Fig. 1h-i, Fig. 2a, d-e). We measured optical transmission for these aqueous carbon suspensions and found a minimum concentration (0.02 g C/mL H₂O) for zero light transmission (300-3400 nm) for a cell thickness of 4 mm (Extended Data Fig. 10, Fig. 3b). We measured light transmission behind a cell across a complete dispersal and retraction sequence. As expected, transmitted light decreased as a function of pigment fluid area (Extended Data Fig. 7), to decrease interior visible light intensity by 91%, 80% and 67% for maximum injections with flow rates of 0.5, 1.0, and 10.0 mL/min, respectively (Fig. 2l-n, respectively). We can therefore use flow rate to control branching and relative area coverage, modulating light transmission through the cell by 24% for differentially-branched patterns of the same maximum radius (Supplementary Video 2, Extended Data Fig. 3a, Extended Data Fig. 4a). Additionally, by controlling the branching effects of the pattern with viscosity differences (ratios), we modulated light transmission by 12% for patterns of the same radius (Supplementary Video 3, Extended Data Fig. 1a-b, Extended Data Fig. 2a-b, Extended Data Fig. 3b, Extended Data Fig. 4b).

Proportional Fluidic Optical and Thermal Responsiveness

Radiative heat transfer through a building facade is a major contributor to operational cooling and heating costs^{5,69}. Transmitted light through a facade, and the energy that is absorbed and reemitted as heat into or out of a building, must be appropriately regulated. In buildings, the fraction of solar radiation that is transmitted into a building is captured by a solar heat gain coefficient, $SHGC = T_{sol} + A_{sol} \cdot N$, where $T_{sol} = \left\{ \sum_{\lambda=250\text{ nm}}^{2500\text{ nm}} T_{\%} \lambda \right\}$ is the transmission fraction across the solar radiation spectrum on Earth, A_{sol} is the solar absorptance fraction, and N is the inward reemission fraction⁷⁰. Decapods, like the sand fiddler crab, control radiative solar heat gain to thermoregulate by managing the volume of pigment dispersed within their chromatophores⁶¹. Analogously, our fluidic building layers can achieve a variable response to incident light by managing the amount of pigment fluid distributed over their cell areas.

To demonstrate this adaptive and proportional response, we fabricated a multicell facade with 16 independent injection sites, each with a local photosensor and thermocouple (Fig. 3a, c). Using the photosensor input behind each cell, a digital negative feedback system was developed for the pigment fluid to maintain a light transmission setpoint, given variable incident light intensity (Fig. 3g-j). An optical stimulus of 100 lux was directed at each cell (Fig. 3g), triggering a temporary and proportionate response (Fig. 3h). 20 mL of pigment was injected (10 mL/min) across 115 s to shade the sensor and restore optical transmission to a set value of 100 lux (Fig. 3i).

For analogous temperature-driven control, we placed a thermocouple on a PMMA sheet 3 cm behind each cell to control a pigment injection response to temperature (Fig. 3k-n). Visible and infrared (IR) light transmission through the cell from an applied heat source elevated the sensor temperature from 22°C to 38°C, and triggered a 20 mL pigment injection (10 mL/min) within 115 s to shade the sensor. The measured temperature of the uninsulated acrylic sheet returned to 22°C after 16 min (Fig. 3m), demonstrating a thermoregulatory effect governed by optical properties, and generally independent of the thermal conductivity of a building facade. Importantly, it has been estimated that adaptive control over IR light transmission and solar heat gain, as we demonstrate here, in just 18% of total building window stock in the United States could reduce building energy use by around 50%⁷¹.

Spatially-differential Optical Responsiveness

Crucial in the camouflaging, shading, and thermoregulatory efforts of several marine organisms is the coordinated differential response of independent fluidic cells across the skin. In buildings, this localized shading control might be similarly beneficial, where spatially-differentiated shading responses could provide glare control without sacrificing diffuse light transmission, and provide desirable differences in daylight penetration across a large space^{18,19}. We mimicked this local actuation capacity in biology to regulate spatially-varied light transmission in building facades. Regions across a multicell facade were individually illuminated (+100 lux), in a sequential manner, and each responded within 15 s (Fig. 4a-b, Supplementary Video 5). With reversibility and pattern stability in mind, we injected pigment slow enough to avoid branching instability. The resulting stable circular patterns also enabled maximum control over area fraction (0% up to a theoretical maximum of $\pi/4$, or 79%). A similar response was demonstrated post-illumination, as pigment cells contracted to return light transmission to a preset threshold (100 lux). Regions were also differentially illuminated, i.e., as a light intensity gradient, and each of the 16 independent cells responded proportionally in under 100 s (Fig. 4e, Supplementary Video 8, Extended Data Fig. 11, experimental setup demonstrated in Fig. 4g), varying a fluidic response between 0-20 mL. The capacity for differential pigment injections across multiple cells over multiple cycles was also demonstrated in Fig. 4d, and in Supplementary Videos 6-7.

We additionally highlight the possibility for large-area pattern control, generating differential pigmentary responses (Fig. 5b-c) through spatial or injection volume modulation, to match the ‘pixels’ of large digitized, optofluidic displays (simulated in Fig. 5d). This ‘halftone’ effect (analogous to screen printing), where a pixel array with a varied radius or morphology can create the appearance of a gradient, is achieved with high accuracy for a resolution of 40x40 cells (approximately 12x12m² for 30cm devices). Increased spatial resolution can be achieved by varying not only the injection pigment radius, but also the branched morphology. Control of pigment branching allows spatially-programmable variation in area coverage for finer spatial resolution than a series of circular half-tone pixels.

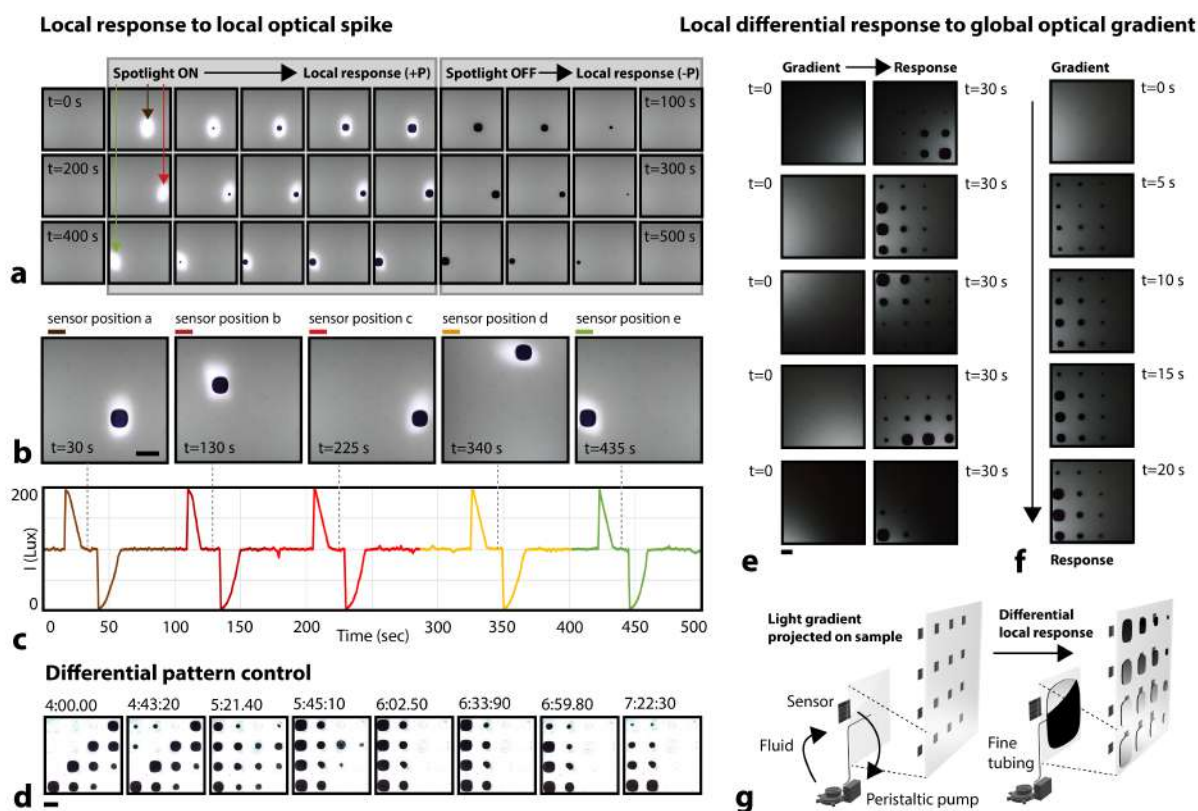


Fig. 4. Differential pigment fluid responsiveness. (a) Independent sequential pigment fluid dispersal/retraction cycles as a response to measured local light intensity behind each cell. Measured value of light intensity drives

negative feedback response for each digitally-driven pump. **(b)** Image captures from Supplementary Video 5, showing localized responses in five independent positions across the facade over time. Scale bars are 10 cm. **(c)** Light intensity as a function of time for five different sensors. **(d)** Image captures from Supplementary Video 6 to demonstrate differential pattern control over time. Scale bar is 10 cm. **(e)** Differential pigment fluid response across all sixteen cells for five independent sequences. Scale bar is 7 cm. **(f)** Second sequence from **(e)**. **(g)** Schematic of experiment in **(e-f)**.

Simulated Building Performance

Digitally-controlled, dynamic fluid interfaces enable a continuous ‘search’ for optimal facade configurations and building operational energy efficiency. To assess the performance impact of our fluidic facade, we leveraged a well-established building energy modelling tool (EnergyPlus) to estimate the annual energy required to heat, cool, and light a conventional commercial space locating in Toronto, Canada (a CAD model is shown in Fig. 6a and more details are described in ⁷²). Within the EnergyPlus model, heating and cooling loads were calculated using the conduction finite difference solution algorithm^{73,74}, based on multi-year environmental data on solar flux, sun position, cloud cover, outdoor temperature, and on input data accounting for the conductivity, emissivity, heat capacity, reflectivity, and absorptivity of all opaque and translucent building materials. We compared annual energy usage for conditioning this modelled space when clad along its south facade with (i) a static double-glazed window (control), (ii) our fluidic facade, (iii) an electrochromic (EC) window, (iv) and a dynamic roller shade (RS) interior to the control window.

We developed a standard control algorithm to simulate the operation of each dynamic system (ii-iv). The algorithm functions as a naïve energy minimizer, restricted to consistently maintain an illuminance of 300 lux (minimum sufficient daylighting) across half of the floor area, and limit an illuminance of 3000 lux (overlighting) to 10% of the floor area. Our fluid window was modelled to switch between eight possible states, derived from the effective solar transmission spectra for our layers with a pigment fluid injection fraction between 0-70% (at 10% steps), within the area fraction limit we observed experimentally (Fig. 6e, green). The EC window was modelled to switch between four optical states (transmission spectra correspond to those of a real market product, and are shown in Fig. 6b, black). The RS was modelled to switch between two optical states (up and down), where the ‘up’ state corresponded to the transmission spectra of the double-pane control window by itself, and the ‘down’ state corresponded to the transmission spectra of the roller shade and control window (Fig. 6b, red). To accurately account for building integration, the fluidic and EC systems were modelled on the exterior, while the RS was modelled on the interior, of the standard control window. This double-glazed control window had a conductive heat transfer coefficient (U-value) of 1.81 W/m²K, a visible transmittance of 0.81, and a SHGC of 0.71. Additional zone details, temperature setpoints, and material properties for our simulation are described in Methods.

In simulation, we found that the dynamic operation of our fluid cell reduced total annual operational energy usage within our commercial space (the sum of heating, cooling, and electric lighting energy usage) by 30.1%, 22.9%, and 20.4% compared to EC, RS, and static double-glazing systems, respectively (Fig. 6j). Because tunable pigment injections allow for significant variability in optical transmission (Fig. 6e), our fluidic device can balance heating, cooling, and lighting loads much more efficiently than any of the other dynamic or static systems. In the winter, for instance, the fluid system can transmit significantly more solar energy than an EC window, leading to large comparative heating energy savings (Fig. 6g). In the summer, on the other hand, our fluid system can block more solar energy, while still achieving minimum daylighting, than a static window or RS system, leading to cooling and electric lighting energy savings (Fig. 6h-i).

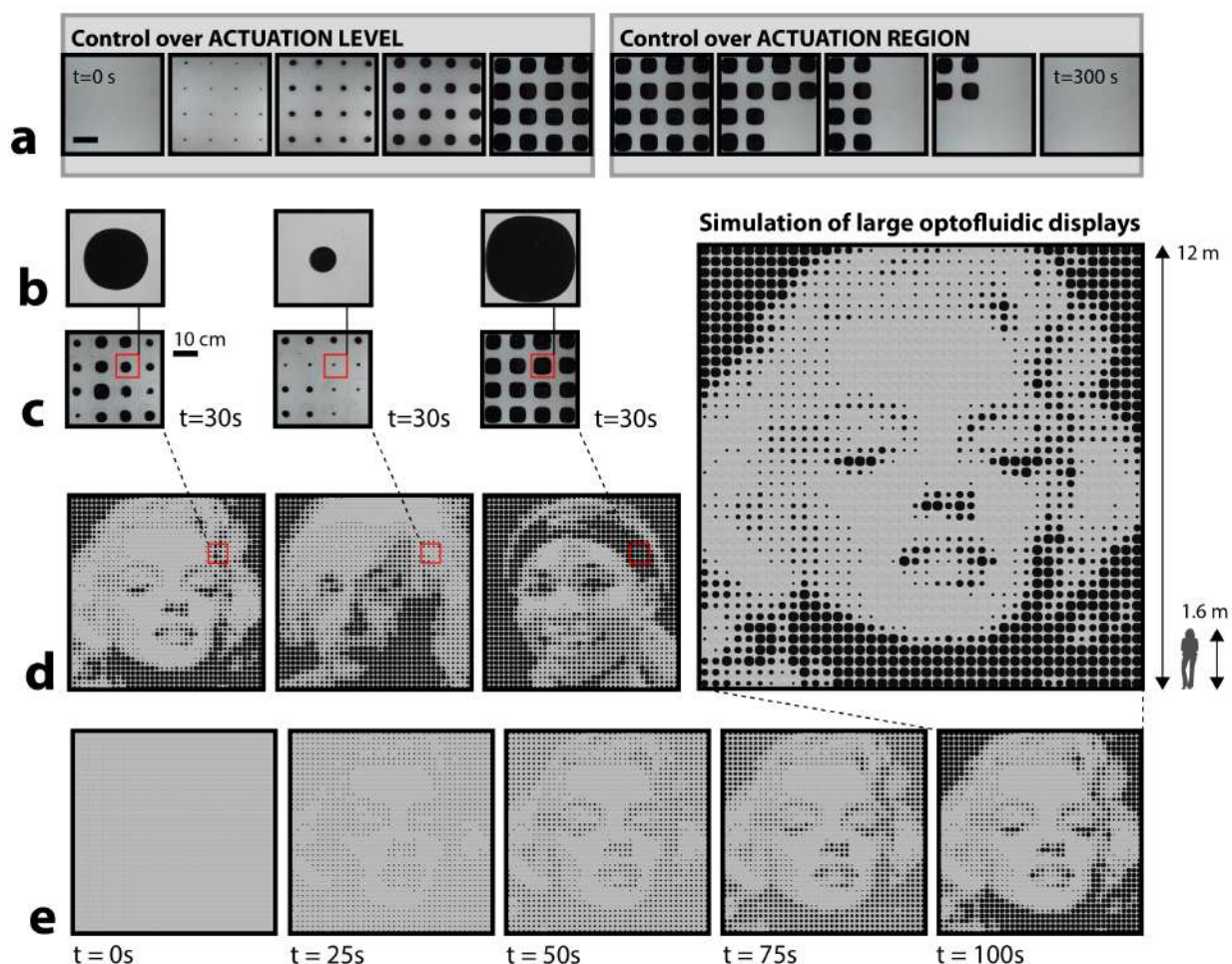


Fig. 5. Envisioned large-area fluidic configurations to display halftone imagery. (a) Demonstrated control over pigment fluid actuation level and region. Scale bar is 10 cm. (b-d) Pattern control at three scales over time. b-c are physically demonstrated; d is simulated. (e) Pattern definition clarity improves over time, as pigment fluid is dispersed differentially.

Operational Temperature Dependence

To estimate the performance capacity of our fluid layer across seasonally-dependent temperatures, we calculated the range in injection velocity required to compensate for the change in relative viscosity induced by the maximum and minimum fluctuations in fluid temperature. Our active fluid layer was implemented on the interior of the previously-described double-glazed control window (U-value of $1.81 \text{ W/m}^2\text{K}$, visible transmittance of 0.81, and SHGC of 0.71), and the temperature of the fluid layer across the year was calculated in EnergyPlus, using the conduction finite difference solution algorithm^{73,74} (Extended Data Fig. 14). The maximum fluid temperature was $44.3 \text{ }^\circ\text{C}$ on August 13th, while the minimum fluid temperature was $8.9 \text{ }^\circ\text{C}$ on February 23rd. We assumed the fluidic pigment to be a water-glycerol solution (0.8/0.2 by volume) with a freezing point of approximately $-10 \text{ }^\circ\text{C}$ ⁷⁵, and we calculated pigment fluid viscosities corresponding to minimum ($8.9 \text{ }^\circ\text{C}$), maximum ($44.3 \text{ }^\circ\text{C}$), and laboratory ($20 \text{ }^\circ\text{C}$) temperatures using the tool developed in⁷⁶, from the relationships described in^{77,78} (Extended Data Table 1). Using known temperature-dependent viscosities for the host mineral oil⁷⁹, we then calculated the viscosity difference to be expected at each relevant fluid temperature within our fluid layer. Accordingly, using the relationships introduced in Equation (2-3), we estimated the required increase or decrease to injection velocity in order to achieve the same

characteristic wavelength as for a laboratory temperature condition with the same fluids. From Extended Data Table 1, we can observe that the estimated change in injection velocity to compensate for minimum and maximum temperature deviations from laboratory conditions is within an order of magnitude: at the coldest modelled annual temperature, the injection velocity would need to be lowered to 43% of its laboratory value, while, at the hottest modelled annual temperature, the injection velocity would need to be raised to 415% of its laboratory value. These changes to injection velocity are well within the functional range of our peristaltic pumps, and we imagine the appropriate temperature-dependent performance could be easily integrated within a digital control algorithm.

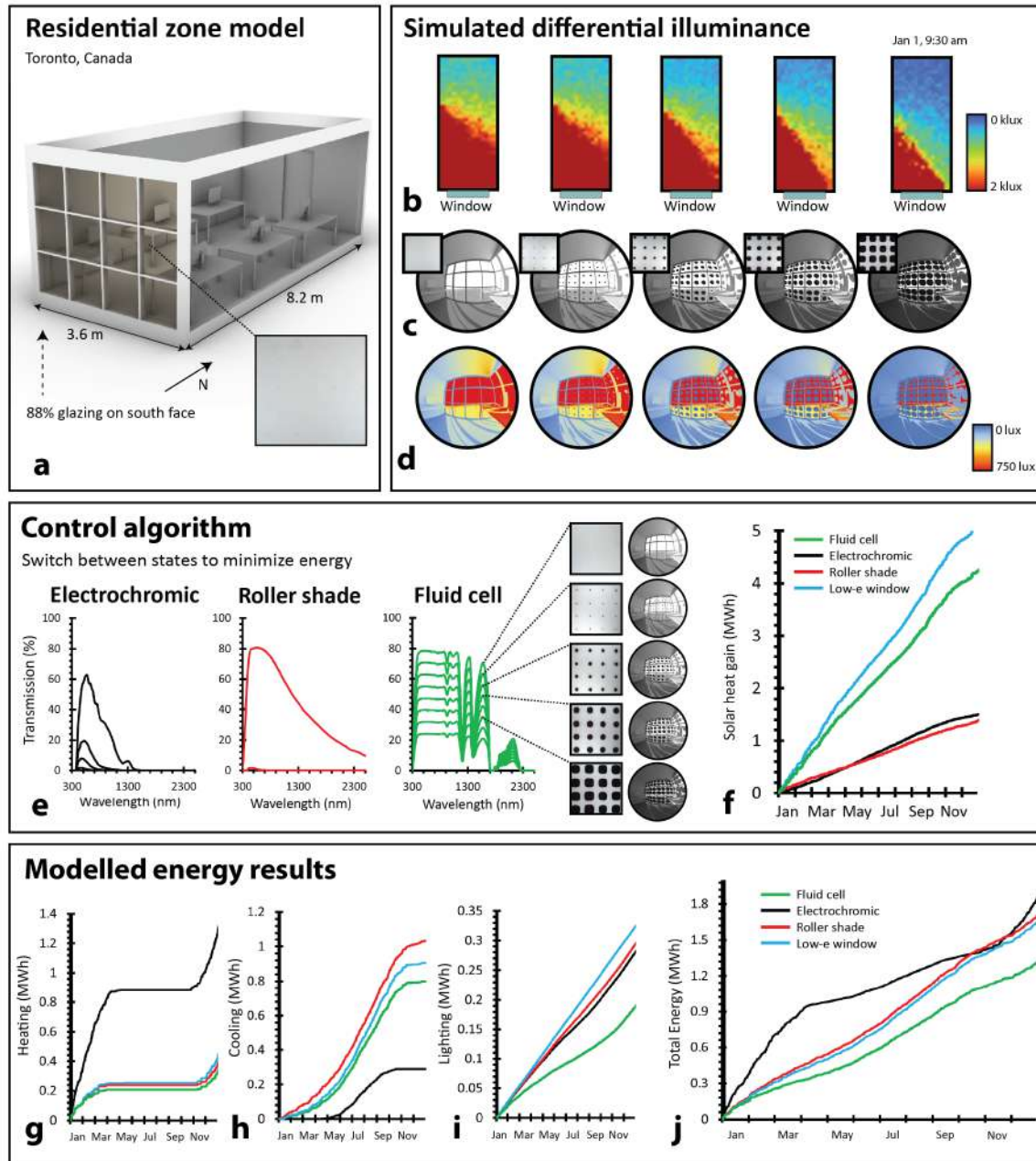


Fig. 6. Simulated system performance and comparative annual energy savings. (a) Commercial zone model for energy simulations, with active south-facing facade. Roof and wall elements were modelled as opaque within the simulation, and appear translucent only for illustration purposes. (b) Spatial illuminance across model floor space at various fluid injection levels. (c-d) Renders within model space at various fluid injection levels, where (c) shows RGB-scale render and (d) shows false-colour render based on illuminance. (e) Transmission spectra of available

optical states for control algorithm to switch between along south facade for EC window, RS, and fluid cell systems. (f) Simulated cumulative solar heat gain, representing the sum of direct and diffuse solar ingress, within the model space across the year when clad with the fluid cell, EC window, RS, and static control window. (g-i) Simulated cumulative heating, cooling, and electric lighting energy usage within the model space across the year when clad with the fluid cell, EC window, RS, and static control window. (j) Total simulated cumulative energy usage within the model space across the year when clad with the fluid cell, EC window, RS, and static control window.

Technoeconomic Feasibility

Our responsive fluidic device can achieve large-area spatiotemporal optical control with low material cost, low embodied energy, simple material processing, and low operational power supply. To assess and quantify the technoeconomic feasibility of our system, we estimated the comparative (i) annual operational energy cost and (ii) material, processing, and fabrication costs of both a state-of-the-art EC window and our active fluidic alternative.

To compare the energy costs for operation, we first estimated the energy required to optimally operate our fluidic facade in our simulation across the year. We calculated the total operational energy as the energy for achieving a complete fluid injection/dispersal sequence within a $\sim 0.25 \text{ m}^2$ panel using our peristaltic pump ($5 \text{ W} \cdot 12 \text{ s}$), multiplied by the number of 0.25 m^2 panels required to glaze the 9.5 m^2 south-facing surface (38), multiplied by the number of injection/retraction events that occur annually in simulation (884), or about 1.4 kWh (0.15 kWh/m^2). This energy cost is less than 0.25% of the total heating, cooling, and lighting energy reduced by our fluid layer over an EC window (578.8 kWh) and is only 30% of a typical operational energy cost estimate of an EC window (0.5 kWh/m^2)^{4,80}. Furthermore, considering a temporal shading rate of 15.6% (i.e., 1364 hours from simulation / 8760 hours), we estimate that other chromogenic systems which require a constant low power supply ($\sim 5 \text{ W/m}^2$) to shade (e.g., liquid-crystal devices³⁵⁻³⁷ and suspended-particle devices^{38,39}) might use 6.82 kWh/m^2 , or about 45 times the operational energy cost of our system.

When considering material, processing, and fabrication energy costs, our trilayer fluid system is remarkably inexpensive, consisting only of two PMMA sheets, off-the-shelf fluids and pigment (castor oil, water, ethanol, carbon black), and off-the-shelf electronics (small peristaltic pump and controller). Including all tubing, electronics, and containment systems, our devices were fabricated for under $\$30 \text{ USD/m}^2$, which, when combined with a typical double-pane window ($\sim \$170 \text{ USD/m}^2$)³¹, would still likely cost under $\$200 \text{ USD/m}^2$. EC systems, on the other hand, rely on energy-intensive multilayer sputter deposition, and are typically fabricated as redox cells consisting of transparent conductors, electrolytes, counter electrodes, and electrochromic films²⁸. Costs of EC devices have decreased substantially over the past two decades, but are still generally in excess of $\$500 \text{ USD/m}^2$, and can be up to $\$1000 \text{ USD/m}^2$, a factor of 2.5-5 greater than our fluid-layer-integrated glazing system²⁷⁻³¹. The embedded energy of EC glazing can also be high, where the production of the conductive, electrolytic, and electrochromic layers can lead to energy costs 25% greater than those for producing a double-glazed, argon-filled unit⁴. We suspect that our fluid system (one mini peristaltic pump and controller, and the small volumes of water, ethanol, and castor oil present) will have only a minimal additional impact on embodied energy. Moreover, the materials in our system can sustain performance over a multidecade lifetime, unsusceptible to ultraviolet degradation present in electrochromics³⁰, with cheap maintenance through easily-replaceable fluidic pigments.

Discussion

Inspired by the dynamic pigment shading response in marine decapods, we demonstrate a low-cost, large-area shading mechanism, leveraging the reversible re-distribution of pigment from a 1D reservoir to 2D area, while organized into independent cells within an array. Analogous to the krill, a small volume of stored pigment fluid (20 mL) can change the overall light transmission of a $30 \times 30 \text{ cm}^2$ area by over 90% when injected and expanded, without an energy requirement to maintain the absorption (shaded) state. While these dynamic optical transitions are much slower than conventional digital displays (seconds to minutes, rather than the $<10 \text{ ms}$ response of a typical LCD display), they fit well within the necessary response time of active building facades in changing solar conditions.

Importantly, buildings are the costliest energy sinks on our planet, consuming approximately 75% of the electricity in the U.S.¹⁶. Any objective to reduce energy efficiencies and total carbon emissions globally should immediately recognize the need for even modest improvements in building design. Despite significant improvements in energy efficiency in certain technologies (e.g., transportation, energy-harvesting), improved building efficiency has progressed only moderately within the past century, and in many respects has even declined. For instance, while the energy costs and inefficiencies of glass windows were recognized since the mid-19th century, our use of glazing in buildings, and the associated indoor heating and cooling costs, has significantly increased^{5,81}.

Buildings with significant glazing ratios must compromise between maximizing total indoor daylight illumination, while limiting localized glare, and the heating and cooling costs year-round. The development of building materials that can find this compromise – i.e., that can actively shade by locally toggling between the optical performance of a window and wall – might simultaneously increase total illumination, reduce concentrated glare and discomfort, and substantially lower mechanical heating and cooling requirements⁷¹. This work represents significant progress in this direction, as we achieve locally-responsive shading that might overcome the functional limitations of macro-scale mechanical mechanisms (e.g., blinds).

Moreover, because the optical properties and functions of fluids can be easily tuned, switchable fluid expansion can be leveraged to control a range of responses beyond binary opaque shading – for example, directionally-programmable light scattering, polarization, and spectrally-selective absorption of IR light (this would crucially decouple control of daylight and heat gain indoors, which is another fundamental challenge in building design). Using a pigment phase that can partially transmit incident light might be more desirable in building applications.

In addition to area fraction control of injected pigment fluid, we leverage an interfacial branching instability to tune morphology. Branching, as opposed to stably expanding, pigment coverage enables larger length-scales of dispersal for small volumes of fluid. Krill achieve branching morphologies through a fixed channel structure, while, in this work, we tune branching dynamically through active control of injection flow rate. Over large areas, branching provides more uniform optical transmission across a window, where multiple branching structures achieve a high spatial resolution of optical consistency, as a halftone response.

Finally, dynamic control over multiple fluidic cells enables highly-localized, digitally-programmable shading responses. Digital control importantly ensures that a ‘whole building response’ can be optimized for maximum energy efficiency in varied hourly, diurnal, and seasonal environmental conditions. In this vein, we showed that fluid reconfigurations at hourly timesteps could achieve massive performance improvements, saving almost 60% on annual heating and cooling energy compared to the static state-of-the-art low-emissivity window. With this fluidic control established, we imagine that artificial intelligence algorithms can collect, processes, and act upon large amounts of localized environmental data, even more drastically improving system management and energy efficiency. Ultimately, there is great potential for digitally-controlled, active shading to allow the next generation of buildings to *learn*, with fundamental implications for an architecture that designs and redesigns itself.

References

- 1 Loonen, R. C. G. M., Trčka, M., Cóstola, D. & Hensen, J. L. M. Climate adaptive building shells: State-of-the-art and future challenges. *Renewable and Sustainable Energy Reviews* **25**, 483-493, doi:<https://doi.org/10.1016/j.rser.2013.04.016> (2013).
- 2 Khandelwal, H., Schenning, A. P. H. J. & Debijs, M. G. Infrared Regulating Smart Window Based on Organic Materials. *Advanced Energy Materials* **7**, 1602209, doi:10.1002/aenm.201602209 (2017).
- 3 Wang, Y., Runnerstrom, E. L. & Milliron, D. J. Switchable Materials for Smart Windows. *Annu Rev Chem Biomol Eng* **7**, 283-304, doi:10.1146/annurev-chembioeng-080615-034647 (2016).
- 4 Papaefthimiou, S., Syrrakou, E. & Yianoulis, P. Energy performance assessment of an electrochromic window. *Thin Solid Films* **502**, 257-264, doi:<https://doi.org/10.1016/j.tsf.2005.07.294> (2006).
- 5 Hee, W. J. *et al.* The role of window glazing on daylighting and energy saving in buildings. *Renewable and Sustainable Energy Reviews* **42**, 323-343, doi:<https://doi.org/10.1016/j.rser.2014.09.020> (2015).
- 6 Auerswald, L., Freier, U., Lopata, A. & Meyer, B. Physiological and morphological colour change in Antarctic krill, *Euphausia superba*: a field study in the Lazarev Sea. *Journal of Experimental Biology* **211**, 3850, doi:10.1242/jeb.024232 (2008).
- 7 Robison Jr., W. G. & Charlton, J. S. Microtubules, microfilaments, and pigment movement in the chromatophores of *Palaemonetes vulgaris* (Crustacea). *Journal of Experimental Zoology* **186**, 279-304, doi:<https://doi.org/10.1002/jez.1401860307> (1973).
- 8 Umbers, K. D. L., Fabricant, S. A., Gawryszewski, F. M., Seago, A. E. & Herberstein, M. E. Reversible colour change in Arthropoda. *Biological Reviews* **89**, 820-848, doi:<https://doi.org/10.1111/brv.12079> (2014).
- 9 Brown, F. A. Hormones in the Crustacea Their Sources and Activities (Concluded). *The Quarterly Review of Biology* **19**, 118-143 (1944).
- 10 Perkins, E. B. Color changes in crustaceans, especially in *Palaemonetes*. *Journal of Experimental Zoology* **50**, 71-105, doi:<https://doi.org/10.1002/jez.1400500106> (1928).
- 11 Brown Jr, F. A. Color changes in *Palaemonetes*. *Journal of Morphology* **57**, 317-333, doi:<https://doi.org/10.1002/jmor.1050570202> (1935).
- 12 Josefsson, L. Structure and function of crustacean chromatophorotropins. *General and Comparative Endocrinology* **25**, 199-202, doi:[https://doi.org/10.1016/0016-6480\(75\)90189-6](https://doi.org/10.1016/0016-6480(75)90189-6) (1975).
- 13 Ban, S. *et al.* Effect of solar ultraviolet radiation on survival of krill larvae and copepods in Antarctic Ocean. *Polar Biology* **30**, 1295-1302, doi:10.1007/s00300-007-0290-2 (2007).
- 14 Jarman, S., Elliott, N., Nicol, S., McMinn, A. & Newman, S. The base composition of the krill genome and its potential susceptibility to damage by UV-B. *Antarctic Science* **11**, 23-26, doi:10.1017/S0954102099000048 (1999).
- 15 Craig, S. & Grinham, J. Breathing walls: The design of porous materials for heat exchange and decentralized ventilation. *Energy and Buildings* **149**, 246-259, doi:<https://doi.org/10.1016/j.enbuild.2017.05.036> (2017).
- 16 USDoE. (2015).
- 17 IEA. (2018).
- 18 Boubekri, M., Cheung Ivy, N., Reid Kathryn, J., Wang, C.-H. & Zee Phyllis, C. Impact of Windows and Daylight Exposure on Overall Health and Sleep Quality of Office Workers: A Case-Control Pilot Study. *Journal of Clinical Sleep Medicine* **10**, 603-611, doi:10.5664/jcsm.3780 (2014).
- 19 Hopkinson, R. G. Glare from daylighting in buildings. *Appl Ergon* **3**, 206-215, doi:10.1016/0003-6870(72)90102-0 (1972).
- 20 Tavares, P. F., Gaspar, A. R., Martins, A. G. & Frontini, F. Evaluation of electrochromic windows impact in the energy performance of buildings in Mediterranean climates. *Energy Policy* **67**, 68-81, doi:<https://doi.org/10.1016/j.enpol.2013.07.038> (2014).
- 21 Lee, E. S., DiBartolomeo, D. L. & Selkowitz, S. E. Thermal and daylighting performance of an automated venetian blind and lighting system in a full-scale private office. *Energy and Buildings* **29**, 47-63, doi:[https://doi.org/10.1016/S0378-7788\(98\)00035-8](https://doi.org/10.1016/S0378-7788(98)00035-8) (1998).
- 22 Konstantoglou, M. & Tsangrassoulis, A. Dynamic operation of daylighting and shading systems: A literature review. *Renewable and Sustainable Energy Reviews* **60**, 268-283, doi:<https://doi.org/10.1016/j.rser.2015.12.246> (2016).

- 23 Drozdowski, Z. & Gupta, S. in *Proceedings of the 29th Annual Conference of the Association for Computer Aided Design in Architecture*. 105-109.
- 24 Lienhard, J. et al. Flectofin: a hingeless flapping mechanism inspired by nature. *Bioinspiration & Biomimetics* **6**, 045001, doi:10.1088/1748-3182/6/4/045001 (2011).
- 25 Park, D. et al. Dynamic daylight control system implementing thin cast arrays of polydimethylsiloxane-based millimeter-scale transparent louvers. *Building and Environment* **82**, 87-96, doi:<https://doi.org/10.1016/j.buildenv.2014.07.016> (2014).
- 26 Attia, S. Evaluation of adaptive facades: The case study of Al Bahr Towers in the UAE. *QScience Connect* **2017**, doi:<https://doi.org/10.5339/connect.2017.qgbc.6> (2018).
- 27 Fernández, J. E. Materials for Aesthetic, Energy-Efficient, and Self-Diagnostic Buildings. *Science* **315**, 1807, doi:10.1126/science.1137542 (2007).
- 28 Lampert, C. M. Chromogenic smart materials. *Materials Today* **7**, 28-35, doi:[https://doi.org/10.1016/S1369-7021\(04\)00123-3](https://doi.org/10.1016/S1369-7021(04)00123-3) (2004).
- 29 Lee, E. S. & DiBartolomeo, D. L. Application issues for large-area electrochromic windows in commercial buildings. *Solar Energy Materials and Solar Cells* **71**, 465-491, doi:[https://doi.org/10.1016/S0927-0248\(01\)00101-5](https://doi.org/10.1016/S0927-0248(01)00101-5) (2002).
- 30 Lampert, C. Large-Area Smart Glass And Integrated Photovoltaics. *Solar Energy Materials and Solar Cells* **76**, 489-499, doi:10.1016/S0927-0248(02)00259-3 (2003).
- 31 Gillaspie, D. T., Tenent, R. C. & Dillon, A. C. Metal-oxide films for electrochromic applications: present technology and future directions. *Journal of Materials Chemistry* **20**, 9585-9592, doi:10.1039/C0JM00604A (2010).
- 32 Granqvist, C. G. Electrochromics for smart windows: Oxide-based thin films and devices. *Thin Solid Films* **564**, 1-38, doi:<https://doi.org/10.1016/j.tsf.2014.02.002> (2014).
- 33 Niklasson, G. A. & Granqvist, C. G. Electrochromics for smart windows: thin films of tungsten oxide and nickel oxide, and devices based on these. *Journal of Materials Chemistry* **17**, 127-156, doi:10.1039/B612174H (2007).
- 34 Fernandes, L. L., Lee, E. S. & Ward, G. Lighting energy savings potential of split-pane electrochromic windows controlled for daylighting with visual comfort. *Energy and Buildings* **61**, 8-20, doi:<https://doi.org/10.1016/j.enbuild.2012.10.057> (2013).
- 35 Cupelli, D. et al. Self-adjusting smart windows based on polymer-dispersed liquid crystals. *Solar Energy Materials and Solar Cells* **93**, 2008-2012, doi:<https://doi.org/10.1016/j.solmat.2009.08.002> (2009).
- 36 Drzaic, P. S. Polymer dispersed nematic liquid crystal for large area displays and light valves. *Journal of Applied Physics* **60**, 2142-2148, doi:10.1063/1.337167 (1986).
- 37 Van Konynenburg, P., Marsland, S. & McCoy, J. Solar radiation control using NCAP liquid crystal technology. *Solar Energy Materials* **19**, 27-41, doi:[https://doi.org/10.1016/0165-1633\(89\)90021-X](https://doi.org/10.1016/0165-1633(89)90021-X) (1989).
- 38 Vergaz, R., Pena, J., Barrios, D., Pérez, I. & Torres, J. Electrooptical behaviour and control of a suspended particle device. *Opto-Electronics Review* **15**, 154-158, doi:<https://doi.org/10.2478/s11772-007-0013-9> (2007).
- 39 Vergaz, R., Sánchez-Pena, J.-M., Barrios, D., Vázquez, C. & Contreras-Lallana, P. Modelling and electro-optical testing of suspended particle devices. *Solar Energy Materials and Solar Cells* **92**, 1483-1487, doi:<https://doi.org/10.1016/j.solmat.2008.06.018> (2008).
- 40 Wang, Q., Gossweiler, G. R., Craig, S. L. & Zhao, X. Cephalopod-inspired design of electro-mechano-chemically responsive elastomers for on-demand fluorescent patterning. *Nature Communications* **5**, 4899, doi:10.1038/ncomms5899 (2014).
- 41 Xu, C., Stiubianu, G. T. & Gorodetsky, A. A. Adaptive infrared-reflecting systems inspired by cephalopods. *Science* **359**, 1495, doi:10.1126/science.aar5191 (2018).
- 42 Rossiter, J., Yap, B. & Conn, A. Biomimetic chromatophores for camouflage and soft active surfaces. *Bioinspir Biomim* **7**, 036009, doi:10.1088/1748-3182/7/3/036009 (2012).
- 43 Granqvist, C. G., Lansåker, P. C., Mlyuka, N. R., Niklasson, G. A. & Avendaño, E. Progress in chromogenics: New results for electrochromic and thermochromic materials and devices. *Solar Energy Materials and Solar Cells* **93**, 2032-2039, doi:<https://doi.org/10.1016/j.solmat.2009.02.026> (2009).
- 44 Granqvist, C. G. Transparent conductors as solar energy materials: A panoramic review. *Solar Energy Materials and Solar Cells* **91**, 1529-1598, doi:<https://doi.org/10.1016/j.solmat.2007.04.031> (2007).

- 45 Granqvist, C. G. Chromogenic materials for transmittance control of large-area windows. *Critical Reviews in Solid State and Materials Sciences* **16**, 291-308, doi:10.1080/10408439008242184 (1990).
- 46 Li, X.-H., Liu, C., Feng, S.-P. & Fang, N. X. Broadband Light Management with Thermochromic Hydrogel Microparticles for Smart Windows. *Joule* **3**, 290-302, doi:<https://doi.org/10.1016/j.joule.2018.10.019> (2019).
- 47 Yu, C. *et al.* Adaptive optoelectronic camouflage systems with designs inspired by cephalopod skins. *Proc Natl Acad Sci U S A* **111**, 12998-13003, doi:10.1073/pnas.1410494111 (2014).
- 48 Reichert, S., Menges, A. & Correa, D. Meteorosensitive architecture: Biomimetic building skins based on materially embedded and hygroscopically enabled responsiveness. *Computer-Aided Design* **60**, 50-69, doi:<https://doi.org/10.1016/j.cad.2014.02.010> (2015).
- 49 Wood, D. M., Correa, D., Krieg, O. D. & Menges, A. Material computation—4D timber construction: Towards building-scale hygroscopic actuated, self-constructing timber surfaces. *International Journal of Architectural Computing* **14**, 49-62, doi:10.1177/1478077115625522 (2016).
- 50 Phillips, P. K. & Heath, J. E. Heat exchange by the pinna of the African elephant (*Loxodonta africana*). *Comp Biochem Physiol Comp Physiol* **101**, 693-699, doi:10.1016/0300-9629(92)90345-q (1992).
- 51 Wright, P. G. Why do elephants flap their ears? *South African Journal of Zoology* **19**, 266-269, doi:10.1080/02541858.1984.11447891 (1984).
- 52 Hillis, D. *et al.* *Life: The Science of Biology*. Vol. 12 (Macmillan, 2020).
- 53 Schmidt-Nielsen, K., Dawson, T. J., Hammel, H. T., Hinds, D. & Jackson, D. C. The jack rabbit - a study in desert survival. *Hvalradets Skrifter* **48**, 125-142 (1965).
- 54 Deravi, L. F. *et al.* The structure-function relationships of a natural nanoscale photonic device in cuttlefish chromatophores. *J R Soc Interface* **11**, 20130942-20130942, doi:10.1098/rsif.2013.0942 (2014).
- 55 Mäthger, L. M. & Hanlon, R. T. Malleable skin coloration in cephalopods: selective reflectance, transmission and absorbance of light by chromatophores and iridophores. *Cell and Tissue Research* **329**, 179, doi:10.1007/s00441-007-0384-8 (2007).
- 56 Chatterjee, A., Norton-Baker, B., Bagge, L. E., Patel, P. & Gorodetsky, A. A. An introduction to color-changing systems from the cephalopod protein reflectin. *Bioinspir Biomim* **13**, 045001, doi:10.1088/1748-3190/aab804 (2018).
- 57 Reiter, S. *et al.* Elucidating the control and development of skin patterning in cuttlefish. *Nature* **562**, 361-366, doi:10.1038/s41586-018-0591-3 (2018).
- 58 Williams, T. L. *et al.* Dynamic pigmentary and structural coloration within cephalopod chromatophore organs. *Nature Communications* **10**, 1004, doi:10.1038/s41467-019-08891-x (2019).
- 59 Hanlon, R. T. *et al.* Cephalopod dynamic camouflage: bridging the continuum between background matching and disruptive coloration. *Philos Trans R Soc Lond B Biol Sci* **364**, 429-437, doi:10.1098/rstb.2008.0270 (2009).
- 60 Hendler, G. & Byrne, M. Fine structure of the dorsal arm plate of *Ophiocoma wendti*: Evidence for a photoreceptor system (Echinodermata, Ophiuroidea). *Zoomorphology* **107**, 261-272, doi:10.1007/BF00312172 (1987).
- 61 Silbiger, N. & Munguia, P. Carapace color change in *Uca pugilator* as a response to temperature. *Journal of Experimental Marine Biology and Ecology* **355**, 41-46, doi:<https://doi.org/10.1016/j.jembe.2007.11.014> (2008).
- 62 Saffman, P. G. & Taylor, G. I. The penetration of a fluid into a porous medium or Hele-Shaw cell containing a more viscous liquid. *Proceedings of the Royal Society of London. Series A. Mathematical and Physical Sciences* **245**, 312-329, doi:10.1098/rspa.1958.0085 (1958).
- 63 Homsy, G. M. Viscous Fingering in Porous Media. *Annual Review of Fluid Mechanics* **19**, 271-311, doi:10.1146/annurev.fl.19.010187.001415 (1987).
- 64 Paterson, L. Radial fingering in a Hele Shaw cell. *Journal of Fluid Mechanics* **113**, 513-529, doi:10.1017/S0022112081003613 (1981).
- 65 Bischofberger, I., Ramachandran, R. & Nagel, S. R. An island of stability in a sea of fingers: emergent global features of the viscous-flow instability. *Soft Matter* **11**, 7428-7432, doi:10.1039/C5SM00943J (2015).
- 66 Bischofberger, I., Ramachandran, R. & Nagel, S. R. Fingering versus stability in the limit of zero interfacial tension. *Nature Communications* **5**, 5265, doi:10.1038/ncomms6265 (2014).
- 67 Bensimon, D., Kadanoff, L. P., Liang, S., Shraiman, B. I. & Tang, C. Viscous flows in two dimensions. *Reviews of Modern Physics* **58**, 977-999, doi:10.1103/RevModPhys.58.977 (1986).

- 68 Zheng, Z., Kim, H. & Stone, H. A. Controlling Viscous Fingering Using Time-Dependent Strategies. *Physical Review Letters* **115**, 174501, doi:10.1103/PhysRevLett.115.174501 (2015).
- 69 Ihm, P., Nemri, A. & Krarti, M. Estimation of lighting energy savings from daylighting. *Building and Environment* **44**, 509-514, doi:<https://doi.org/10.1016/j.buildenv.2008.04.016> (2009).
- 70 Curcija, C. *et al.* WINDOW Technical Documentation. (Lawrence Berkeley National Laboratory, 2018).
- 71 DeForest, N. *et al.* United States energy and CO₂ savings potential from deployment of near-infrared electrochromic window glazings. *Building and Environment* **89**, 107-117, doi:<https://doi.org/10.1016/j.buildenv.2015.02.021> (2015).
- 72 Reinhart, C. F., Jakubiec, J. A. & Ibarra, D.
- 73 Ceylan, H. & Myers, G. E. Long-Time Solutions to Heat-Conduction Transients with Time-Dependent Inputs. *Journal of Heat Transfer-transactions of The Asme* **102**, 115-120 (1980).
- 74 Energy, U. S. D. o. EnergyPlus Version 9.5.0 Engineering Reference. (2021).
- 75 Lane, L. B. Freezing Points of Glycerol and Its Aqueous Solutions. *Industrial & Engineering Chemistry* **17**, 924-924, doi:10.1021/ie50189a017 (1925).
- 76 Partridge, M. (2018).
- 77 Volk, A. & Kähler, C. J. Density model for aqueous glycerol solutions. *Experiments in Fluids* **59**, 75, doi:10.1007/s00348-018-2527-y (2018).
- 78 Cheng, N.-S. Formula for the Viscosity of a Glycerol–Water Mixture. *Industrial & Engineering Chemistry Research* **47**, 3285-3288, doi:10.1021/ie071349z (2008).
- 79 Paar, A. (2021).
- 80 Syrrakou, E., Papaefthimiou, S. & Yianoulis, P. Environmental assessment of electrochromic glazing production. *Solar Energy Materials and Solar Cells* **85**, 205-240, doi:<https://doi.org/10.1016/j.solmat.2004.03.005> (2005).
- 81 Pérez-Lombard, L., Ortiz, J. & Pout, C. A review on buildings energy consumption information. *Energy and Buildings* **40**, 394-398, doi:<https://doi.org/10.1016/j.enbuild.2007.03.007> (2008).
- 82 Chen, Y. M. & Pearlstein, A. J. Viscosity-temperature correlation for glycerol-water solutions. *Industrial & Engineering Chemistry Research* **26**, 1670-1672, doi:10.1021/ie00068a030 (1987).
- 83 Segur, J. B. & Oberstar, H. E. Viscosity of Glycerol and Its Aqueous Solutions. *Industrial & Engineering Chemistry* **43**, 2117-2120, doi:10.1021/ie50501a040 (1951).
- 84 Takamura, K., Fischer, H. & Morrow, N. R. Physical properties of aqueous glycerol solutions. *Journal of Petroleum Science and Engineering* **98-99**, 50-60, doi:<https://doi.org/10.1016/j.petrol.2012.09.003> (2012).
- 85 Canada, N. R. C. (2017).

Methods

Prototype Fabrication and Preparation

Several prototype devices were fabricated, ranging in surface area from 5x5 cm² to 45x45 cm². All prototypes were fabricated as PMMA-liquid-PMMA sandwiches (Hele-Shaw cells, 1-mm fluid gap). For single-cell devices, an inlet hole (5.5 mm diameter) was drilled into one of the PMMA plates, and a luer adapter with a barbed hose fitting was sealed to the inlet using two-part epoxy resin. PVC tubing (1/4" I.D., 3/8" O.D.) was connected to a digital peristaltic pump (INTLLAB, RS385-635) or digital syringe pump (New Era Pump Systems, NE-1010) for experimentation. The space between rigid plates was sealed with a 1-mm-thick sheet of double-sided tape (3M), which acted as a durable and waterproof boundary for the enclosed liquid layer. An outlet hole (5.5 mm diameter) was drilled to allow air to escape during filling.

The devices were first filled with transparent host liquid (oil). Experiments were conducted by pumping pigment fluids into the oil-filled cell. If both plates of the cell were rigid (in this case made of 3-mm-thick PMMA), four outlets were established (one at each corner of the cell, 5.5 mm diameter). Each outlet enabled a small volume of liquid to reversibly leak and return, into a container open to the atmosphere. This method was used for pattern morphology testing, as plate thickness could be kept constant (plate thickness impacts branching pattern features). For multi-cell prototypes, a thinner PMMA plate (0.2 mm thick) was used to alleviate the need for outlets. All PMMA sheets were transparent, however a white sheet of plastic was placed directly behind the cell to

observe fluidic patterning more clearly. All PMMA sheets were either milled using a three-axis CNC-mill (XYZ Pacer 4010 ATC) or cut with a laser cutter (Universal Laser Systems PLS 6.150D). The tape gasket was cut manually.

Fluid Preparation and Viscosity Measurements

We used castor mineral oil (Heritage Store) as the clear host liquid. We used different glycerol-water (BioShop, purity 99%) solutions with suspended carbon black particles (Davis Colors, 0.2 g C per 50 mL glycerol-water solution) as the pigmented liquid. Mixtures were sonicated (iSonic D3200) for 120 seconds. Viscosities of glycerol-water solutions were calculated using the four-parameter correlation of temperature dependence on aqueous glycerol solution viscosities, presented by Chen and Pearlstein⁸², and were further verified by comparing our calculated values to experimental values measured by Segur and Oberstar⁸³. The viscosity of the carbon suspension in water was measured using a Cannon-Fenske capillary viscometer (Sigma-Aldrich Z275301), and was found to be identical to water by itself (1 cP). The viscosity of castor oil was also measured using the viscometer (288 cP), and confirmed with⁷⁹.

Density Matching Experiments

To eliminate buoyancy differences, we used a water/ethanol solution (23 vol%) as a guest fluid to match the density of the host fluid (castor oil) at 23 °C (0.95 g/mL). Mixing of these miscible liquids does not result in a significant change in partial molar volumes⁸⁴. Experiments with vertical devices confirmed there were no drifting effects observed over multiple-hour-long periods.

Branching Pattern Characterization and Flow Rate Measurements

Branching fluidic patterns were characterized based on the number and thickness of branches formed for various flow rates. Fluid area coverage was calculated in ImageJ (NIH, United States). The number of branches were counted and marked in Rhinoceros3D (McNeel, United States). Radius was measured based on a circle that fully enclosed all branching features. Pattern perimeter was measured digitally in Rhinoceros. Characteristic wavelength was determined based on the thickness of the most unstable wavelength – that is half of the width of a finger branch at the moment before it begins to split, as described in previous work⁶⁵. For viscosity tests, an inner and outer circle was defined, respectively, as a circle that completely enclosed the inner fluidic area, and as a circle that completely enclosed all fluidic features. These were identified and defined manually, and their radii, perimeters, and areas were measured digitally in Rhinoceros. Flow was generated and measured using a NE-1010 digital syringe pump. A syringe was connected to inlet PVC tubing (1/4" I.D., 3/8" O.D.), which connected the pressurized syringe to the cell.

Light Intensity Measurements and Electronic Feedback

We programmed an Arduino MEGA 2560 R3 (Elegoo) to translate the output of a simple photosensor (Adafruit 161) into a proportional input for a 12V DC digital peristaltic pump (INTLLAB RS385-635). We used a handheld LED light source (Neewer 10095736) to provide a constant light intensity of 100 lux. For single-sensor experiments, we used an Extech HD450 Light Meter Datalogger, placed behind our cell, to measure and log light intensity. Light intensity reduction values were calculated as percentage reductions, by taking the difference in visible light intensity (measured behind the cell) prior to, and after, complete fluid injection, and dividing this number by the maximum visible light intensity measured prior to injection.

Temperature Measurements and Electronic Feedback

We programmed an Arduino MEGA 2560 R3 (Elegoo) to translate the output of a digital K-type thermocouple (HiLetGo) into a proportional input for a 12V DC digital peristaltic pump (INTLLAB RS385-635). The experimental setup is detailed in Fig. 3k. We used an incandescent light bulb as a heat source that generated a constant power of 100 W. We used a K-type thermocouple (0.523 kJ/kgK) to measure the temperature of a PMMA sheet (1.42 kJ/kgK), 3 cm behind the fluidic facade.

Optical Spectral Measurements

UV-vis-infrared spectrophotometry (Perkin-Elmer Lambda 1050) was performed for both clear and pigment fluids.

Local and Differential Light Intensity Control and Electronic Feedback

We connected one digital peristaltic pump (INTLLAB RS385-635) to the inlet tubing for every cell, and placed a photosensor (Adafruit 161) 2 cm behind each cell to measure cell-specific local light intensity. We applied a similar control algorithm as described for individual cells, and illuminated individual cells in sequence to generate a fluidic pigment response to independent local light intensity changes.

Simulated Optofluidic Displays

A Python program was developed to first input and convert RGB images as greyscale multipixel arrays, next average regional collections of greyscale pixels, and finally replace multipixel collections with experimental images of fluid injection. We replaced greyscale pixels with images of our fluid injection experiment. For smaller pixel greyscale values (closer to black), we replaced the pixel with an image of a fluid injection after a longer time (i.e., more fluid displaced). In particular, we sorted the pixels into 5 buckets and proportionally matched up the pixels with experimental images of varying degrees of injection. As a result, we generated several half-tone displays using experimental images of stable, quasi-circular, injection sequences.

Building Energy Simulation Control Algorithm

At every hour that the modelled space was occupied, each dynamic control state (Fig 6e) was tested for the preset daylighting requirements (illuminance of 300 lux across at least half of the floor area, and an illuminance above 3000 lux across less than 10% of the floor area). For every state that met these requirements, electric lighting utilization and solar heat gains were calculated, followed by a heat balance at each hour based on model outputs for internal heat gains (occupants, lights, equipment) and external heat gains (ventilation, solar heat gains, conduction). At each hour, of all the tested states, the state that minimized total heating, cooling, and electric lighting energy was selected. Finally, to account for the transient nature of the thermal model, the control algorithm was iterated many times until the annual energy results stabilized at a near-optimal solution.

Simulation Parameters

EnergyPlus was used to simulate annual energy usage within a previously defined commercial reference space, described in ⁷². A standard hourly occupancy schedule was assumed for the space ⁸⁵, with an occupancy density of 0.0538 m²/person. Non-exterior walls, floors, and ceilings were set as adiabatic. Opaque walls were modelled with a U-value of 0.472 W/m²K, and we used standard IES LM-83 values to describe other indoor materials. A fresh air supply of 0.0125 m³/s/person was used, and we assumed that 70% of sensible heat and 65% of latent heat was recovered by the heat-recovery system. Each person generated 125 W of heat, and indoor equipment was modelled with a maximum power density of 5 W/m², and an hourly schedule defined by the National Energy Code of Canada for Buildings. ⁸⁵ Temperature setpoints were defined at 21 and 24 °C when the space was occupied, and at 15.6 and 26.7 °C otherwise. An electric lighting power of 99 W (3.4 W/m²) across the space was assumed. Finally, lights were activated daily between 7:00-19:00, and were dimmed to meet a target illuminance while optimizing thermal gains.

Acknowledgments:

We acknowledge the help of Ethan Heimlich for developing the fluidic visualization algorithm. We also thank Nicholas Hoban for his conceptual and technical input early on in the project.

Funding:

Canadian Foundation for Innovation (CFI) #31799 (BDH)

Percy Edward Hart Professorship, University of Toronto (BDH)

RK was supported by a Canada Graduate Scholarship, a C.W. Bowman Graduate Scholarship, and a Bert Wasmund Graduate Fellowship.

Author contributions:

Conceptualization: RK, CK, BDH

Methodology: RK, CK, KN, BDH

Physical experimentation: RK

Simulation and control algorithm design: JAJ

Visualization: RK

Electronic system design: KN

Funding acquisition: BDH

Writing – first draft: RK

Editing and revision: RK, CK, KN, JAJ, BDH

Additional Information

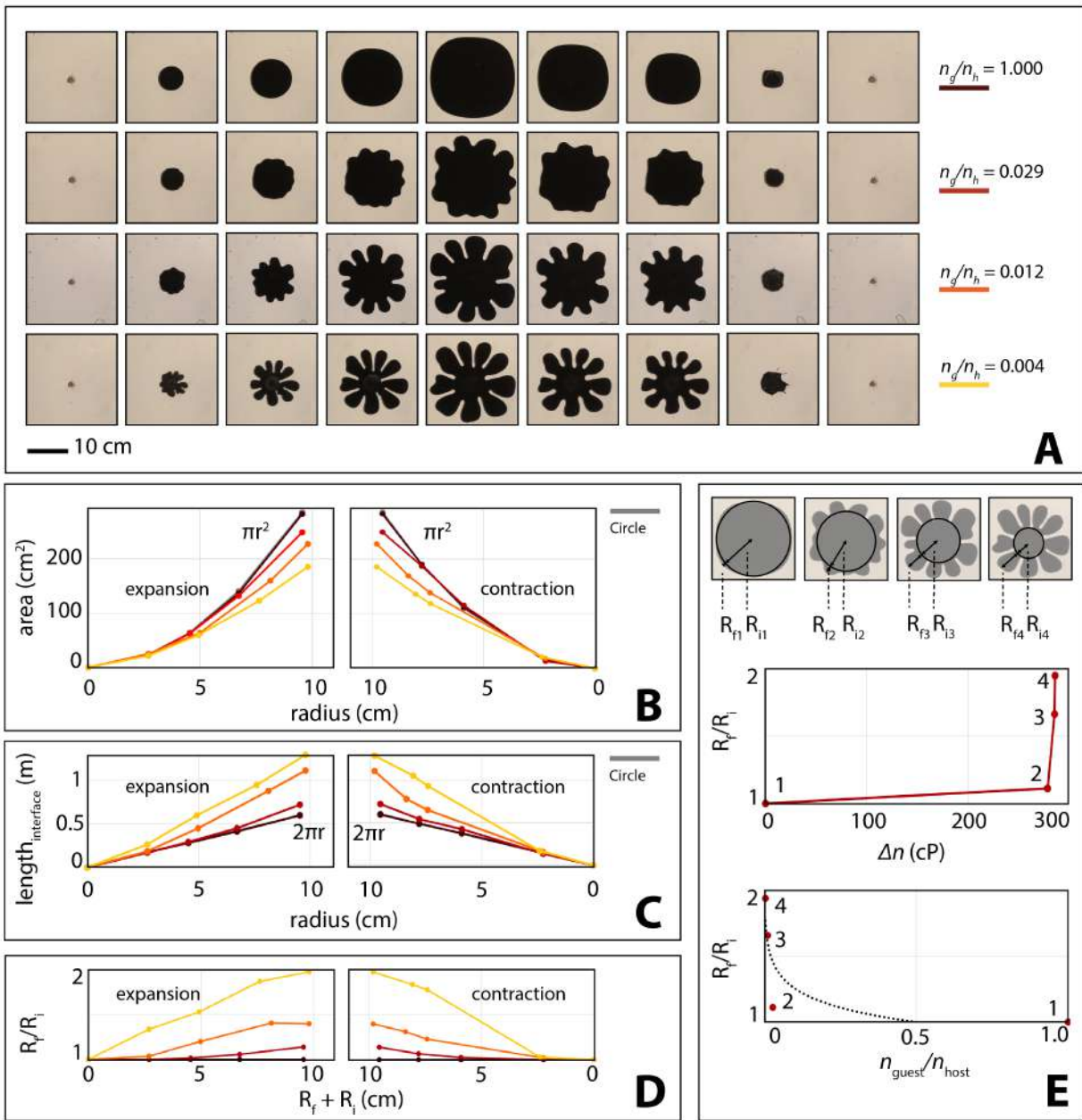
Supplementary Information is available for this paper.

Correspondence and requests for materials should be addressed to raphael.kay@mail.utoronto.ca,

Reprints and permissions information is available at www.nature.com/reprints.

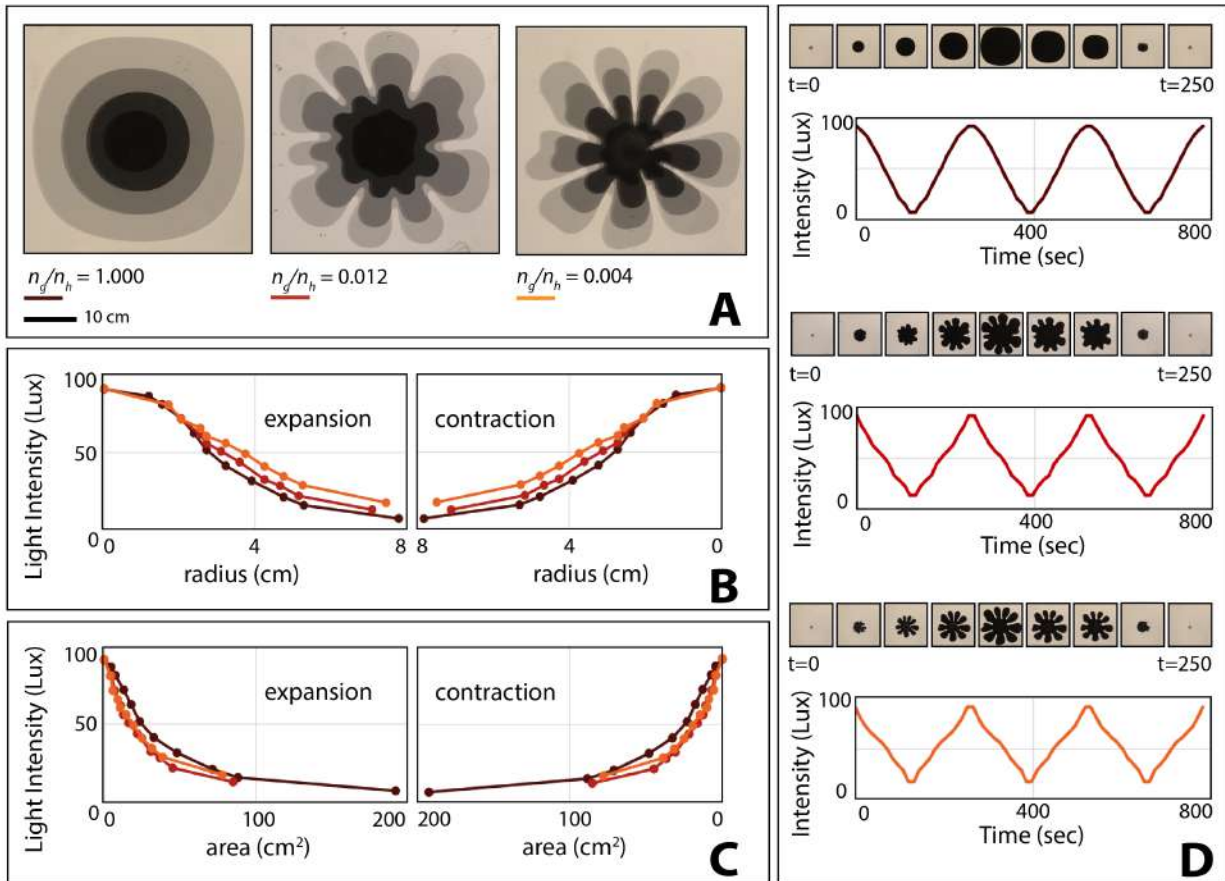
Competing interests: Authors declare that they have no competing interests.

Data and materials availability: All data will be made available by the authors upon request.



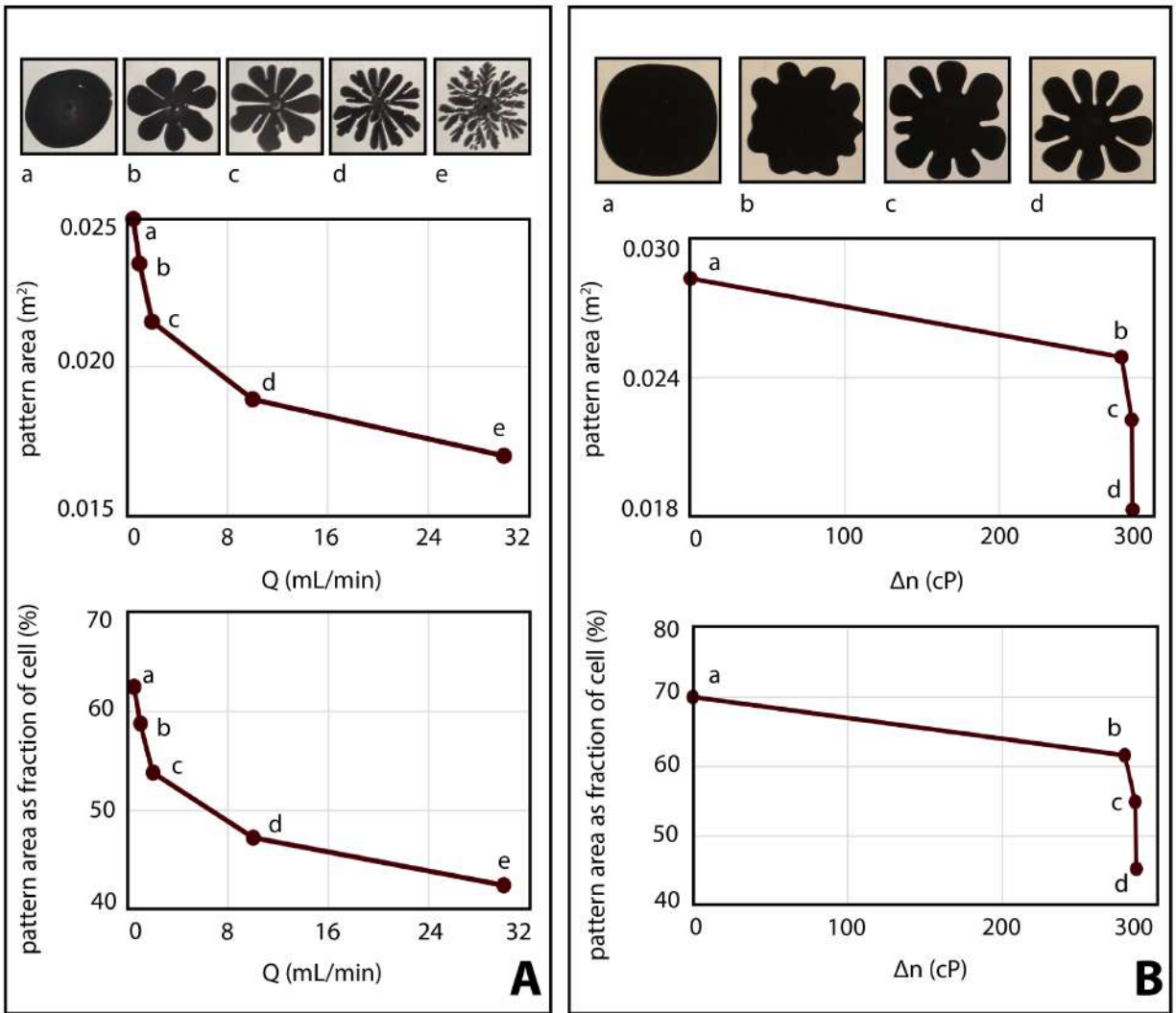
Extended Data Fig. 1.

Control over geometrical characteristics of pigment dispersal through tuning of ratio between viscosity of guest fluid (n_g) and viscosity of host fluid (n_h). (a) Four individual pigment injection and retraction sequences, from left to right, over time, with varied ratio between guest and host fluid viscosities. (b) Area of pigment formation as function of pattern radius through expansion and contraction sequence. (c) Interfacial perimeter of pigment formation as function of pattern radius through expansion and contraction sequence. (d) Ratio of circular radii corresponding to inner (R_i) and fingering (R_f) pattern regions as function of total pattern radius. (e) Ratio of circular radii corresponding to inner (R_i) and fingering (R_f) pattern regions as function of viscosity difference and ratio.



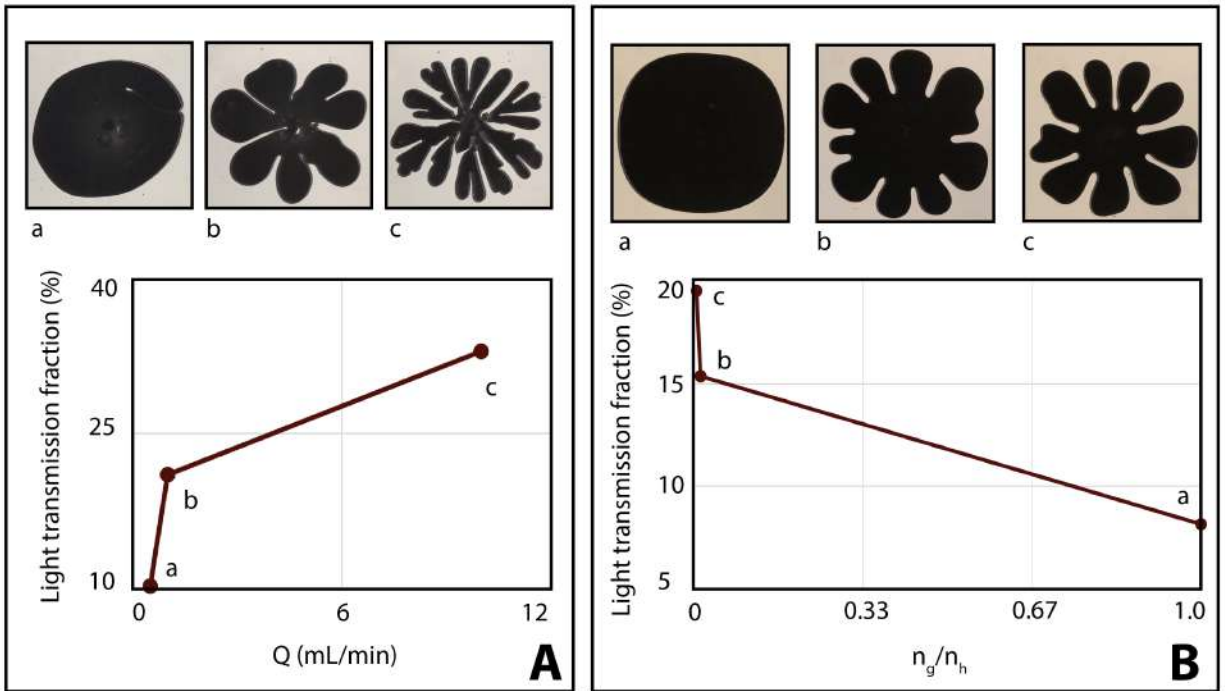
Extended Data Fig. 2.

Indirect effect of viscosity difference on light transmission. (a) Overlaid time-series images for three independent pigment injection sequences, where viscosity difference (and ratio) is varied. (b) Relative transmitted light intensity through the Hele-Shaw cell as function of pattern radius. (c) Relative transmitted light intensity as function of pattern area. (d) Light intensity as function of time across three repeated pattern injection and retraction sequences.



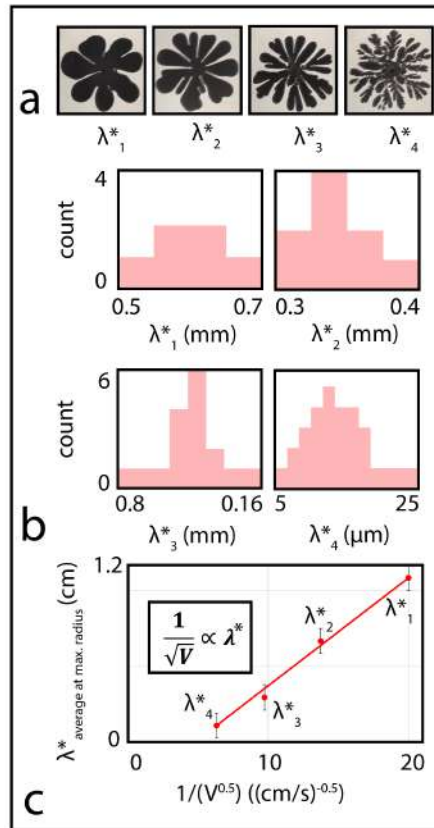
Extended Data Fig. 3.

Tuning of pattern area as function of flow rate (a) and viscosity difference (b) for patterns of a comparable radius within a Hele-Shaw cell.



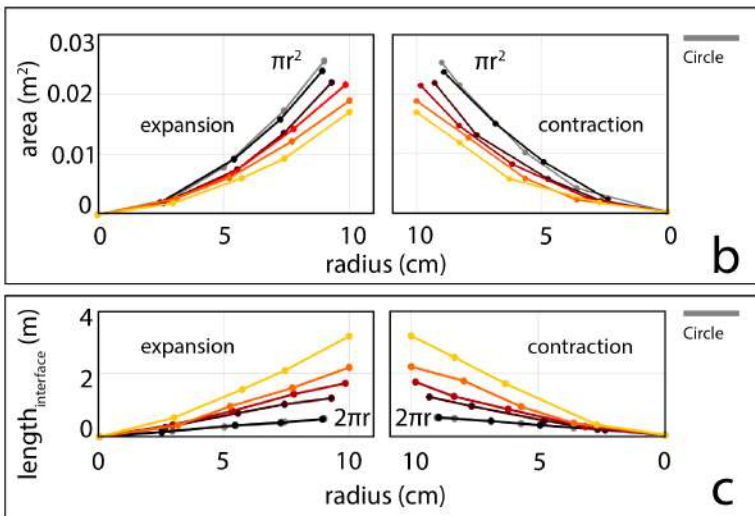
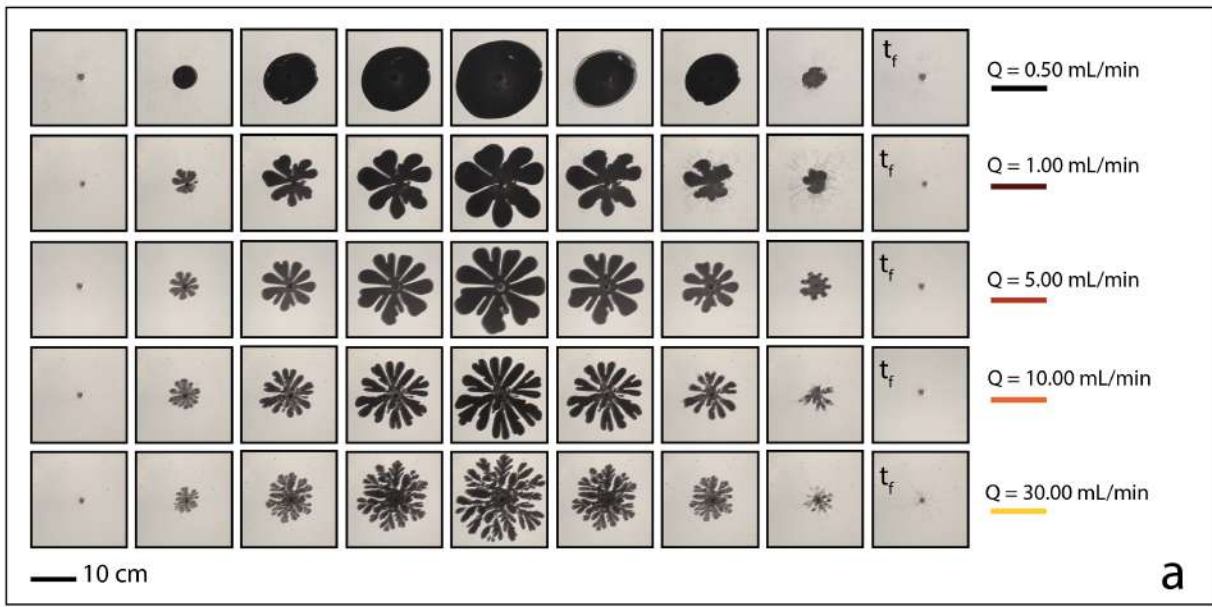
Extended Data Fig. 4.

Tuning of light transmission through Hele-Shaw cell for different pattern morphologies as a function of flow rate (a) and viscosity ratio (b). All patterns have an equivalent maximum radius.



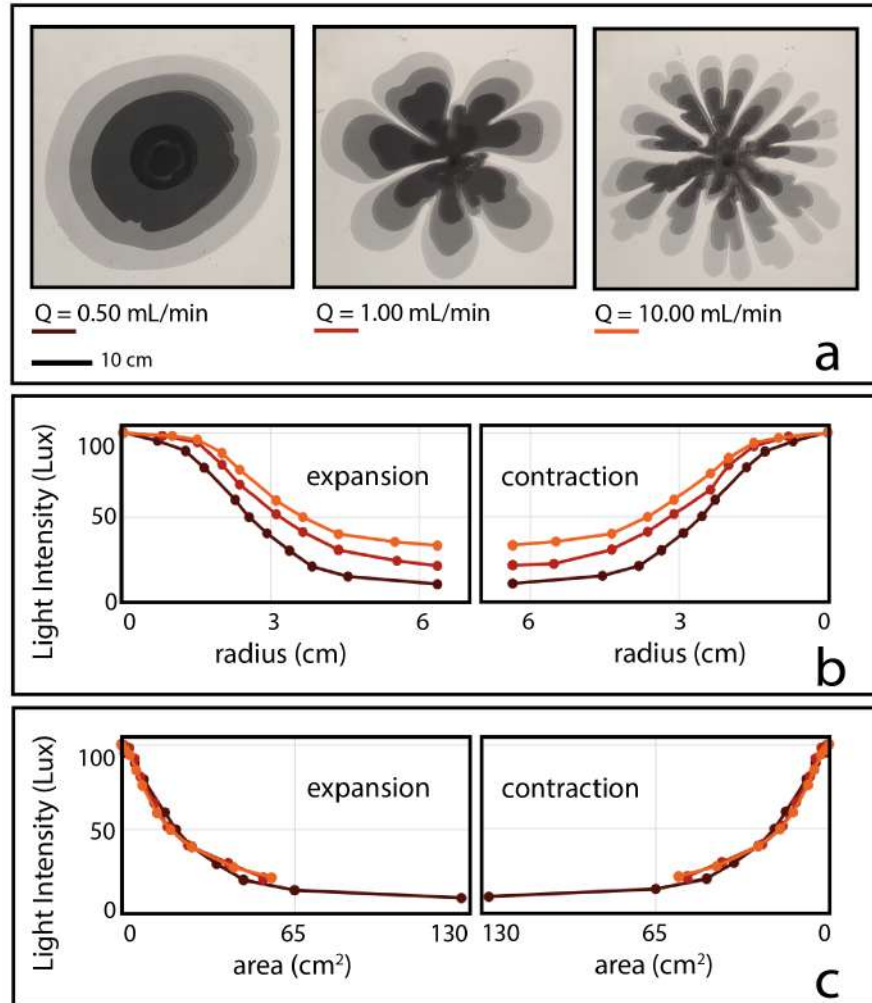
Extended Data Fig. 5.

Observed pattern morphology is consistent with equations (2-3), where the characteristic wavelength is proportional to the inverse of the square of V , the observed interfacial velocity (c). Here, the characteristic wavelength (λ^*) is taken as the average wavelength of fingers observed in (a).



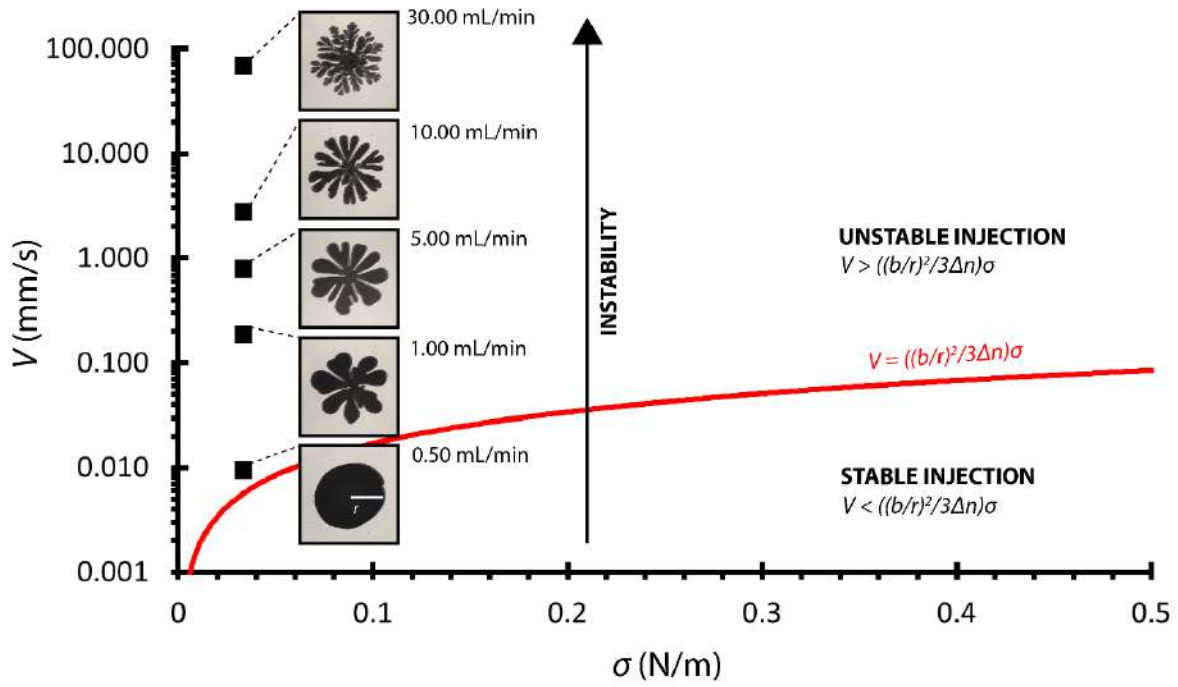
Extended Data Fig. 6.

Control over geometrical characteristics of pigment dispersal through tuning of flow rate. (a) Five individual pigment injection and retraction sequences, from left to right, over time, with varied flow rates. (b) Area of pigment formation as function of pattern radius through expansion and contraction sequence. (c) Interfacial perimeter of pigment formation as function of pattern radius through expansion and contraction sequence.



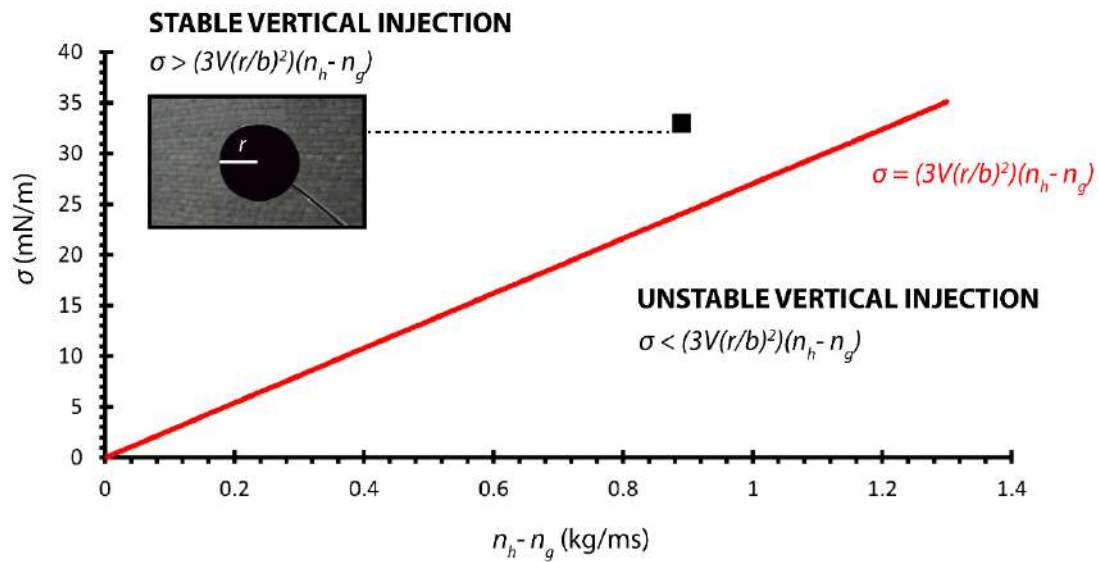
Extended Data Fig. 7.

Indirect effect of flow rate on light transmission. (a) Overlaid time-series images for three independent pigment injection sequences, where flow rate is varied. (b) Relative transmitted light intensity through Hele-Shaw cell as function of pattern radius. (c) Relative transmitted light intensity as function of pattern area. Light transmission is dependent only on pattern area.



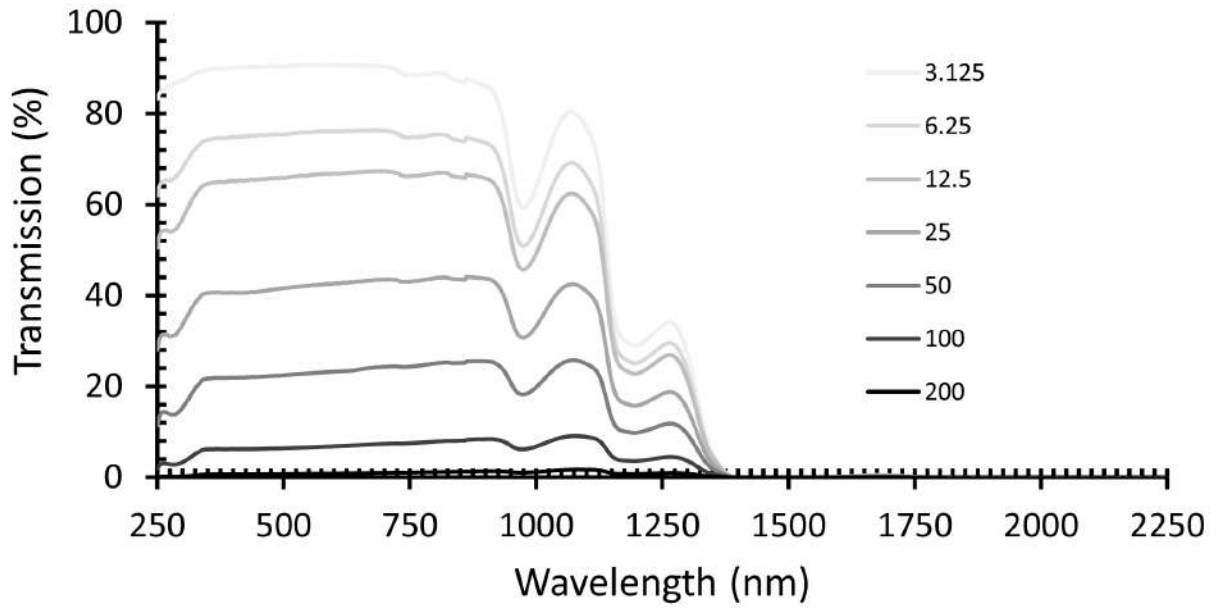
Extended Data Fig. 8.

Binary phase space differentiating between stable and unstable pigment injections within a Hele-Shaw cell. One can observe the decrease in characteristic finger width λ^* as the value of V increases, further away from the region of stability. At higher values of σ , greater velocities are needed to support unstable branched growth.



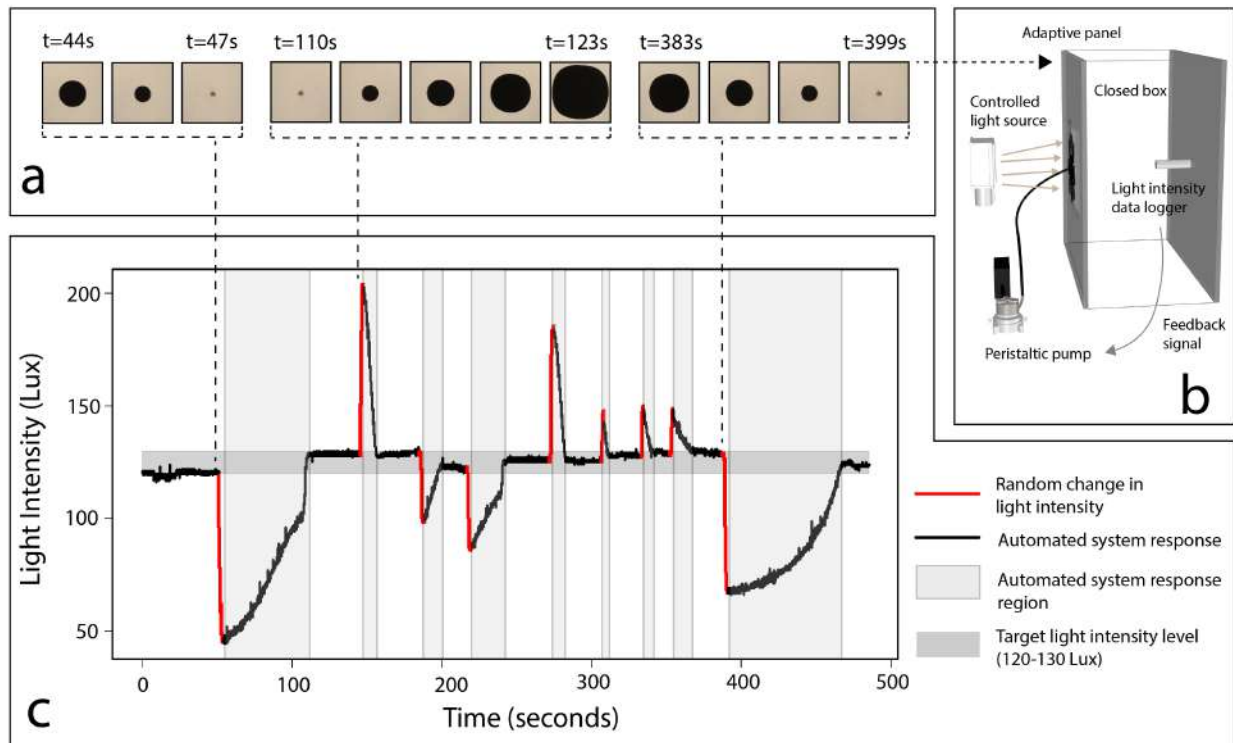
Extended Data Fig. 9.

Binary phase space for stable non-branching and unstable branching pigment injection within a vertical Hele-Shaw cell.



Extended Data Fig. 10.

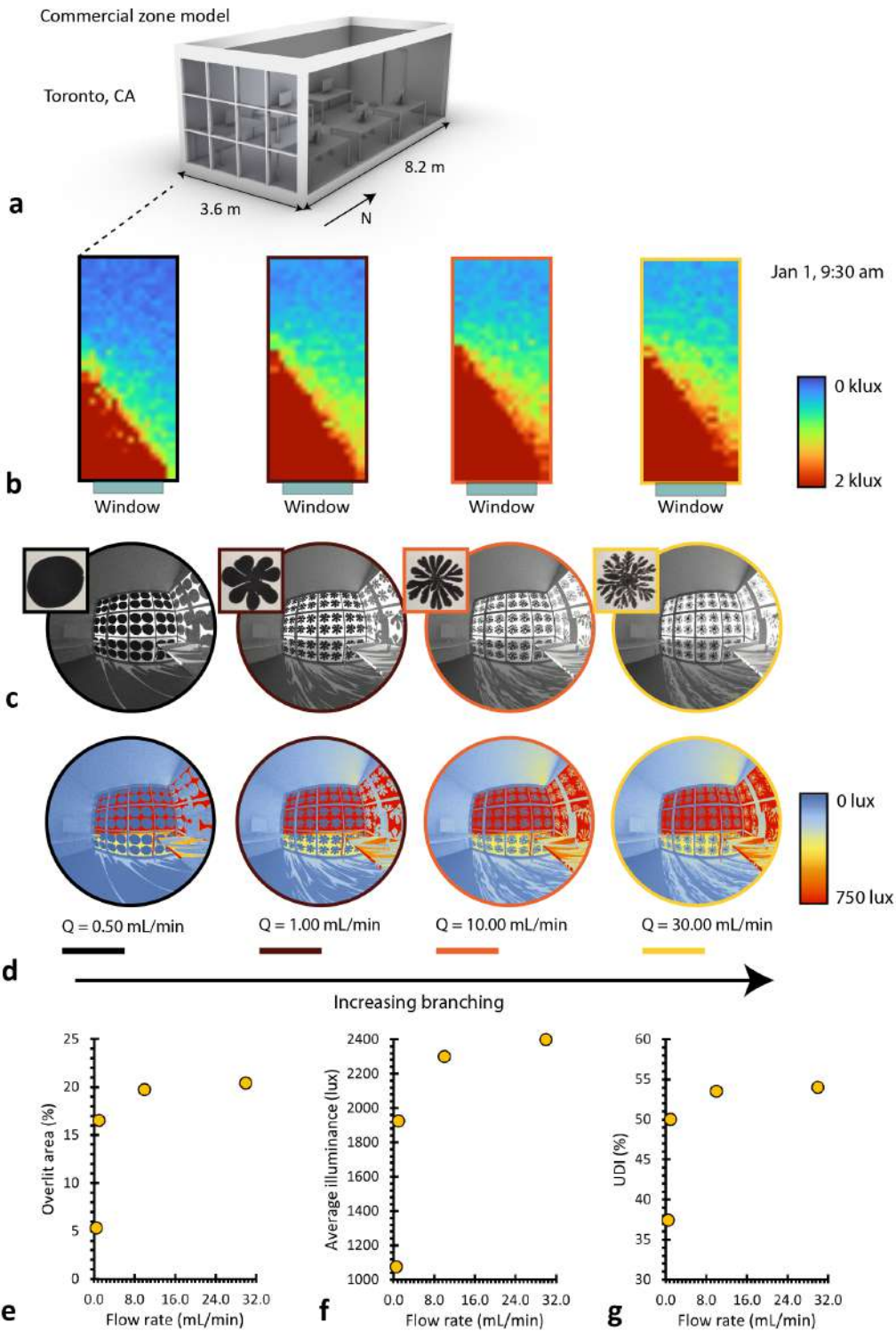
Optical transmission for various aqueous suspensions of carbon black, for a 4-mm-thick fluidic optical path length. Values describe concentration of mg carbon per 50 mL of H₂O.



Extended Data Fig. 11.

Demonstration of negative optical feedback system. (a) Examples to illustrate pigment fluid response. (b) Schematic of experiment. (c) Measured interior light intensity, where red curves represent manual interventions to

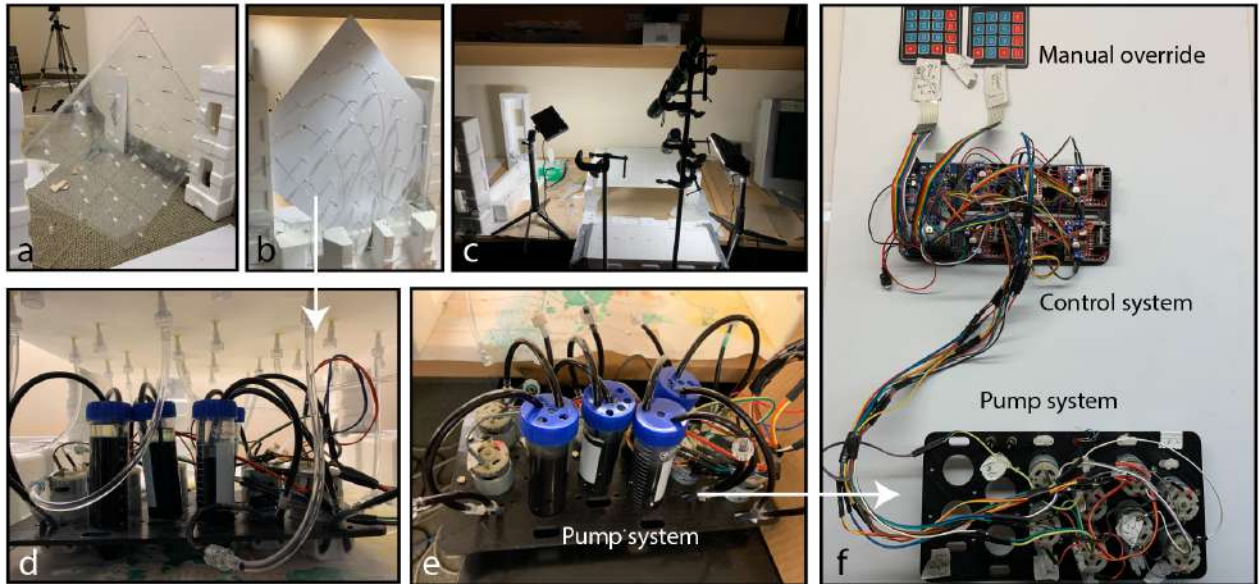
increase or decrease light intensity, and black curves represent digital optical response to change in measured light intensity.



Extended Data Fig. 12.

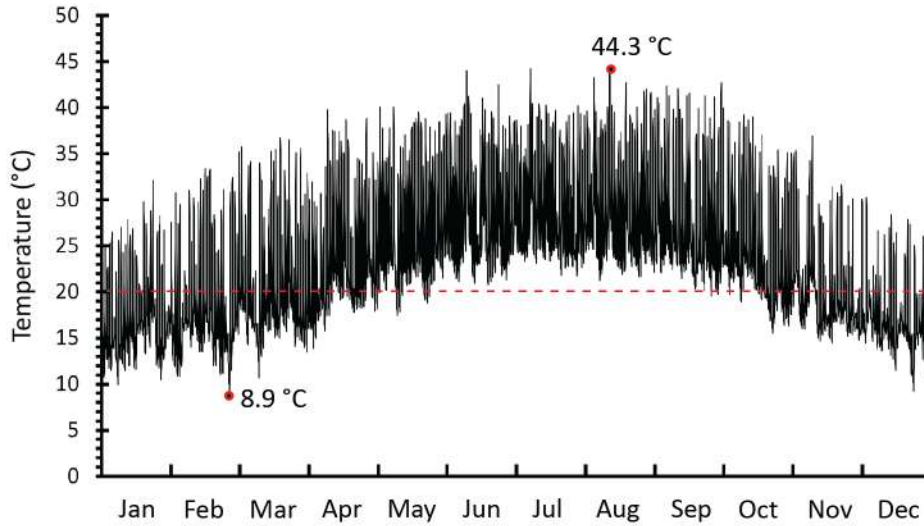
Differences in indoor illumination for maximum pigment injections at different flow rates (different viscous fingering patterns). (a) Model used for daylight simulation. (b) Illuminance distribution across space (sensors

spaced every 0.2 m, and modelling plane taken at 0.762 m). (c-d) Renderings within room taken on Jan 1 at 9:30 am, where (c) shows RGB render and (d) shows false colour render. (e) Degree of branching within fluid injection determines percentage of space defined as over-lit (>1000 lux of direct incident light). (f) Degree of branching within fluid injection determines average illuminance of space. (g) Degree of branching within fluid injection determines percentage of space defined as usefully lit (indicated here by a useful daylight illuminance fraction, or as the % of space lit at > 300 lux).



Extended Data Fig. 13.

Photographs of experiments and devices. (a-b) Vertical multicell panels, rotated 45° for oil bubble avoidance during preliminary oil injection. (c) Horizontal panel with targeted light intensity gradient setup. (d) Fluid pump system connected to panel. White backdrop added behind panels in (b-d) for better contrast during imaging. (e) Fluid panel system, disconnected from panel. (f) Electronics design, including fluid pump system, control system, and manual override system. Input light sensor wiring not pictured.



Extended Data Fig. 14.

Simulated fluid temperature across the year, when modelled on inside of control double-glazed window in Toronto, Canada, as calculated using the conduction finite difference solution algorithm in EnergyPlus. The maximum fluid temperature was 44.3 °C on August 13th, and the minimum fluid temperature was 8.9 °C on February 23rd. The dashed red line denotes laboratory temperature of 20 °C. Using this data, we calculated the expected change in viscosity difference and the change in injection velocity required to appropriately compensate for these viscosity changes induced by temperature deviations.

Extended Data Table 1.

Required change in velocity to account for seasonal temperature fluctuations

Condition	T (°C)	T - T _{lab} (°C)	n _g (Pa · s)	n _h (Pa · s)	Δn (Pa · s)	required V (mm/s) for constant λ _c	Required increase to V for constant λ _c
Laboratory	20.0	0.0	0.00188	0.28723	0.28535	1.000 (arbitrary)	0%
Winter	8.9	-11.1	0.00281	0.66495	0.66214	0.431	-57%
Summer	44.3	+24.3	0.00110	0.06974	0.06864	4.158	316%